

## QUANTUM PROCESSES IN SHORT AND INTENSIVE ELECTROMAGNETIC FIELDS

*A. I. Titov*<sup>1,\*</sup>, *B. Kämpfer*<sup>2,3</sup>, *A. Hosaka*<sup>4,5</sup>, *Hideaki Takabe*<sup>2,6</sup>

<sup>1</sup> Joint Institute for Nuclear Research, Dubna

<sup>2</sup> Helmholtz-Zentrum Dresden–Rossendorf, Dresden, Germany

<sup>3</sup> Institut für Theoretische Physik, TU Dresden, Dresden, Germany

<sup>4</sup> RCNP, 10-1 Mihogaoka Ibaraki, Osaka, Japan

<sup>5</sup> J-PARC Branch, KEK, Tokai, Ibaraki, Japan

<sup>6</sup> ILE, Yamada-oka, Suita, Osaka, Japan

INTRODUCTION	836
ENVELOPE FUNCTIONS	841
THE $e^+e^-$ PAIR PRODUCTION IN A FINITE PULSE	846
COMPTON SCATTERING IN SHORT LASER PULSE	874
SUMMARY	890
Appendix	
PRODUCTION PROBABILITY AT LARGE VALUES OF $\xi$	893
REFERENCES	896

---

\*E-mail: atitov@theor.jinr.ru

## QUANTUM PROCESSES IN SHORT AND INTENSIVE ELECTROMAGNETIC FIELDS

*A. I. Titov*<sup>1,\*</sup>, *B. Kämpfer*<sup>2,3</sup>, *A. Hosaka*<sup>4,5</sup>, *Hideaki Takabe*<sup>2,6</sup>

<sup>1</sup> Joint Institute for Nuclear Research, Dubna

<sup>2</sup> Helmholtz-Zentrum Dresden-Rossendorf, Dresden, Germany

<sup>3</sup> Institut für Theoretische Physik, TU Dresden, Dresden, Germany

<sup>4</sup> RCNP, 10-1 Mihogaoka Ibaraki, Osaka, Japan

<sup>5</sup> J-PARC Branch, KEK, Tokai, Ibaraki, Japan

<sup>6</sup> ILE, Yamada-oka, Suita, Osaka, Japan

This work provides an overview of our recent results in studying two most important and widely discussed quantum processes: electron–positron pair production off a probe photon propagating through a polarized short-pulsed electromagnetic (e.g., laser) wave field or generalized Breit–Wheeler process, and a single photon emission off an electron interacting with the laser pulse, the so-called nonlinear Compton scattering. We show that the probabilities of particle production in both the processes are determined by interplay of two dynamical effects, where the first one is related to the shape and duration of the pulse, and the second one is nonlinear dynamics of the interaction of charged fermions with a strong electromagnetic field. We elaborate suitable expressions for the production probabilities and cross sections, convenient for studying evolution of the plasma in presence of strong electromagnetic fields.

Представлен обзор последних результатов в исследовании двух наиболее важных и широко обсуждаемых квантовых процессов: образования электрон-позитронных пар при прохождении внешнего фотона через поляризованный электромагнитный (лазерный) пучок, или обобщенного процесса Брейта–Уиллера, и излучения фотонов при взаимодействии электрона с лазерным импульсом — так называемого нелинейного комптоновского рассеяния. Показано, что вероятности образования частиц в обоих процессах определяются комбинацией двух динамических эффектов, один из которых связан с формой и длительностью импульса, а второй — с нелинейной динамикой взаимодействия заряженных фермионов с сильным электромагнитным полем. Получены формулы расчета вероятностей и поперечных сечений образования частиц, удобные для исследования эволюции плазмы в присутствии сильных электромагнитных полей.

PACS: 12.20.Ds; 13.40.-f; 23.20.Nx

---

\*E-mail: atitov@theor.jinr.ru

## INTRODUCTION

The rapidly progressing laser technology [1] offers unprecedented opportunities for investigations of quantum systems with intense laser beams [2]. A laser intensity  $I_L$  of  $\sim 2 \cdot 10^{22}$  W/cm<sup>2</sup> has been already achieved [3]. Intensities of the order of  $I_L \sim 10^{23} - 10^{25}$  W/cm<sup>2</sup> are envisaged in the near future, e.g., at the CLF [4], ELI [5], HiPER [6]. Further facilities are in planning on construction stage, e.g., PEARL laser facility [7] at Sarov/Nizhny Novgorod, Russia. The high intensities are provided in short pulses on a femtosecond pulse duration level [2, 8, 9], with only a few oscillations of the electromagnetic (e.m.) field or even subcycle pulses. In order to achieve such high intensities in the focal spot of the laser beam, a crucial technique is required. (The tight connection of high intensity and short pulse duration is further emphasized in [10]. The attosecond regime will become accessible at shorter wavelengths [11, 12].)

Quantum processes occurring in the interactions of charge fermions in very (infinitely) long e.m. pulse were investigated in detail in the pioneering works of Reiss [13, 14] as well as Narozhny, Nikishov, and Ritus [15, 16] and some other papers (see, for example, [17]). We call such approaches as an infinite pulse approximation (IPA) since it refers to a stationary scattering process. Many simple and clear expressions for the production probabilities and cross sections have been obtained within IPA. It was shown that the charged fermion (electron, for instance) can interact with  $n \geq 1$  photon simultaneously ( $n$  is an integer number), and cases with  $n > 1$  correspond to the subthreshold, multiphoton events. However, since the new laser generation is expected to operate with the finite (short and ultra-short) pulses, the question naturally arises whether predictions of IPA are valid for the finite pulses or not.

Indeed, recently it was shown that for the photon production off an electron interacting with short laser pulse (Compton scattering) in [10, 18–24], and for  $e^+e^-$  pair production off a probe photon interacting with short e.m. pulses (Breit–Wheeler process) in [25–29], the finite pulse shape and the pulse duration become important. That means, the treatment of the intense and short laser field as an infinitely long wave train is no longer adequate. The theory must operate with essentially finite pulse. We call such approaches as a finite pulse approximation (FPA). Formation of positrons from cascade processes in a photon–electron–positron plasma [30, 31] generated by photon–laser [32], electron–laser [33, 34] or laser–laser interactions [35] (see [36, 37] for surveys) is an important problem in laser physics. The evaluation of corresponding transport equations needs, as an input, the probabilities/cross sections for the production of energetic photons (e.g., in the nonlinear Compton scattering) and direct emission of  $e^+e^-$  pairs (e.g., in the nonlinear Breit–Wheeler process).

Consider first the nonlinear Breit–Wheeler process. Corresponding linear Breit–Wheeler  $e^+e^-$  pair production  $\gamma' + \gamma \rightarrow e^+ + e^-$  [38] refers to a perturbative

QED reaction; the generalization to the multiphoton process  $\gamma' + n\gamma \rightarrow e^+ + e^-$  (nonlinear Breit–Wheeler process) in IPA was done in [13, 16, 17]. Attributing these processes to colliding null fields, one can imagine another aspect. In the antinode of suitably counter propagating e.m. waves, an oscillating purely electric field can give rise to the dynamical Schwinger effect [39]; in the low-frequency limit one recovers the famous Schwinger effect [40] awaiting still its experimental verification. These kinds of pair creation processes are related to highly nonperturbative effects [41, 42]. Once pair production is seeded in very intense fields, further avalanche-like particle production could screen the original field or even limit the attainable field strength [30]. One can relate the Breit–Wheeler process to the absorptive part of the probe-photon correlator in an external e.m. field; in our case the latter being a null field, too. Later, we focus on colliding null fields in the multiphoton regime and consider the generalized Breit–Wheeler effect for short pulses of e.m. wave fields ranging from weak to high intensities. Phrased differently, we analyze  $e^+e^-$  pair production by a probe photon  $\gamma'$  traversing a coherent e.m. (i.e., laser) field. We employ the four-potential of a circularly polarized laser field in the axial gauge  $A^\mu = (0, \mathbf{A}(\phi))$  with

$$\mathbf{A}(\phi) = f(\phi) \left( \mathbf{a}_1 \cos(\phi + \tilde{\phi}) + \mathbf{a}_2 \sin(\phi + \tilde{\phi}) \right), \quad (1)$$

where  $\phi = k \cdot x$  is invariant phase with four-wave vector  $k = (\omega, \mathbf{k})$ , obeying the null field property  $k^2 = k \cdot k = 0$  (a dot between four-vectors indicates the Lorentz scalar product) implying  $\omega = |\mathbf{k}|$ ,  $\mathbf{a}_{(1,2)} \equiv \mathbf{a}_{(x,y)}$ ;  $|\mathbf{a}_x|^2 = |\mathbf{a}_y|^2 = a^2$ ,  $\mathbf{a}_x \mathbf{a}_y = 0$ ; transversality means  $\mathbf{k} \mathbf{a}_{x,y} = 0$  in the present gauge. The envelope function  $f(\phi)$  with  $\lim_{\phi \rightarrow \pm\infty} f(\phi) = 0$  (FPA) accounts for the finite pulse length. (IPA would mean  $f(\phi) = 1$ .) To define the pulse duration, one can use the number  $N$  of cycles in a pulse,  $N = \Delta/\pi = (1/2)\tau\omega$ , where the dimensionless quantity  $\Delta$  or the duration of the pulse  $\tau$  are further useful measures. The carrier envelope phase  $\tilde{\phi}$  is particularly important if it is varied in a range comparable with the pulse duration  $\Delta$ . In IPA it is anyhow irrelevant; in FPA with  $\tilde{\phi} \simeq \Delta$  the cross section of the photon emission would be determined by an involved interplay of the carrier phase, the pulse duration, and pulse shape as well as the intensity of e.m. field as emphasized, e.g., in [43]) (see also [28, 44]). In the beginning, we drop the carrier phase, thus assuming  $\tilde{\phi} \ll \Delta$ , and concentrate on the dependence of the cross sections on the parameters responsible essentially for multiphoton effects. Impact of  $\tilde{\phi}$  on the differential production rate is discussed in Subsecs. 2.7 and 3.4. In present consideration we drop effect of the pulse focusing which, however, is more relevant for longer pulses [45] than those covered in the present review where we consider pulses with the number of oscillations less than ten.

The interaction of an electron with e.m. field is characterized by the dimensionless field intensity  $\xi^2$ . For simplicity, let us consider the case of generalized Compton scattering, where the variable  $\xi^2$  can be determined through the average value of the manifestly covariant variable  $\eta = T^{\mu\nu} p_\mu p_\nu / (p \cdot k)^2$  [46] (cf. also [15]), where  $p$  is the four-momentum of a target electron, and  $T^{\mu\nu}$  is the e.m. stress-energy tensor  $T^{\mu\nu} = g_{\alpha\beta} F^{\mu\alpha} F^{\beta\nu} + (1/4)g^{\mu\nu} F_{\alpha\beta} F^{\alpha\beta}$ , where  $F_{\mu\nu} = \partial_\mu A_\nu - \partial_\nu A_\mu$  stands for the e.m. field strength tensor. In the charge's rest frame  $\eta = T^{00}/\omega^2$ , where the stress-energy tensor  $T^{00}$  is equal to the energy density of the e.m. field or to the pulse intensity  $I_L$ . In IPA, the quantity  $\xi^2$  is determined by

$$\xi^2 = \frac{e^2}{m^2} \frac{1}{\tau_{\text{IPA}}} \int_{-\tau_{\text{IPA}}/2}^{\tau_{\text{IPA}}/2} dt \eta = \frac{e^2}{m^2 \omega^2} \frac{1}{2\pi} \int_{-\pi}^{\pi} d\phi I_L = \frac{e^2 a^2}{m^2}, \quad (2)$$

where the averaging interval is set equal to the duration of one cycle,  $\tau_{\text{IPA}} = 2\pi/\omega$  (we use natural units with  $c = \hbar = 1$ ,  $e^2/4\pi = \alpha \approx 1/137.036$ ). The generalization to a finite pulse may be done in a straightforward manner:

$$\xi_{\text{FPA}}^2 = \frac{e^2}{m^2} \frac{1}{\tau_{\text{FPA}}} \int_{-\infty}^{\infty} dt \eta = \frac{e^2}{m^2 \omega^2} \frac{1}{2\pi N} \int_{-\infty}^{\infty} d\phi I_L. \quad (3)$$

Now, the interval  $\tau_{\text{FPA}}$  is determined by the number  $N$  of oscillations in a pulse as  $2\pi N/\omega$ . That is, the quantity  $\xi^2$ , which defines the production probability and the cross section, can be expressed through the averaged value of the intensity of a finite laser pulse

$$\xi^2 = \xi_{\text{FPA}}^2 \frac{N}{N_0}, \quad (4)$$

or

$$\begin{aligned} \xi^2 &= \frac{N}{N_0} \frac{e^2}{\omega^2 m^2} \langle I_L \rangle \simeq \frac{N}{N_0} \frac{5.62 \cdot 10^{-19}}{\omega^2 [\text{eV}^2]} \langle I_L \rangle \left[ \frac{\text{W}}{\text{cm}^2} \right], \\ &\simeq \frac{N}{N_0} 3.66 \cdot 10^{-19} \lambda^2 [\mu\text{m}^2] \langle I_L \rangle \left[ \frac{\text{W}}{\text{cm}^2} \right], \end{aligned} \quad (5)$$

where  $\lambda = 2\pi/\omega$  is the wave length of the background field and  $N_0 \langle I_L \rangle = (\omega/2\pi) \int_{-\infty}^{\infty} dt I_L$ . Hence, the normalization factor  $N_0$  is determined as

$$N_0 = \frac{1}{2\pi} \int_{-\infty}^{\infty} d\phi (f^2(\phi) + f'^2(\phi)) \quad (6)$$

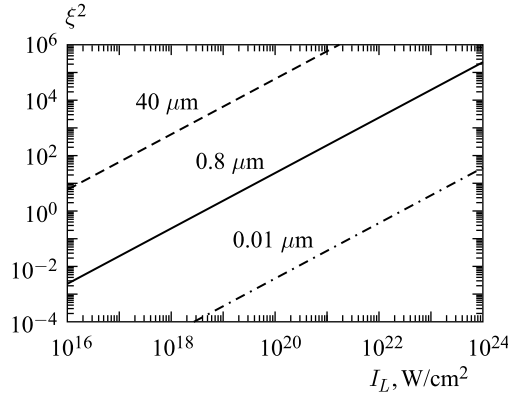


Fig. 1. Reduced field intensity  $\xi^2$  as a function of averaged pulse intensity  $I_L$  for different wave lengths. Dashed, solid, and dash-dotted curves are for  $\lambda = 40, 0.8,$  and  $0.01 \mu\text{m}$ , respectively

and has a meaning of renormalized factor for the photon flux in the case of finite pulse. The factor  $N_0$  is described in some detail below in Sec. 1. In fact, for the realistic envelope functions  $N_0 \simeq N$  and, therefore,  $\xi^2 \simeq \xi_{\text{FPA}}^2$ . The generalization to the Breit–Wheeler process can be done straightforwardly by substitution  $p \rightarrow k'$  and utilizing the center-of-mass system (c.m.s.).

For completeness, in Fig. 1 we exhibit explicit dependence of  $\xi^2$  on  $I_L$  for different wave lengths for  $N = N_0$ . Dashed, solid, and dash-dotted curves are for  $\lambda = 40, 0.8,$  and  $0.01 \mu\text{m}$ , respectively, which correspond to the infrared, optic, and X-ray scales.

The second relevant dimensionless variable characterizing both null fields is

$$\zeta = \frac{s_{\text{thr}}}{s}, \quad (7)$$

where  $s_{\text{thr}} = 4m^2$  and  $s = 2\omega\omega'(1 - \cos \Theta_{\mathbf{k}\mathbf{k}'})$  (for head-on collision geometry,  $\Theta_{\mathbf{k}\mathbf{k}'} = \pi$ );  $\omega, \omega'$  and  $\mathbf{k}, \mathbf{k}'$  are the frequencies and three-wave vectors of the laser field and the probe photon, respectively. The variable  $s_{\text{thr}}$  is the square of the initial energy at the threshold, therefore, the variable  $\zeta$  is a pure kinematic quantity with the meaning that for  $\zeta > 1$  the linear Breit–Wheeler process  $\gamma' + \gamma \rightarrow e^+ + e^-$  is subthreshold, i.e., kinematically forbidden. However, multiphoton effects enable the nonlinear process  $\gamma' + n\gamma \rightarrow e^+ + e^-$  even for  $\zeta > 1$  which we refer as subthreshold pair production. The nonlinear Breit–Wheeler process has been experimentally verified in the experiment E-144 at SLAC [47]. There, the minimum number of photons involved in one  $e^+e^-$  event can be estimated by the integer part of  $\zeta(1 + \xi^2)$ , i.e., five. To arrive at such an estimate, we recall that the reduced strength  $\xi$  is related to the laser intensity  $I_L$  via Eq. (5),

and therefore, at  $\omega' = 29$  GeV,  $\omega = 2.35$  eV, and at peak focused laser intensity of  $1.3 \cdot 10^{18}$  W/cm<sup>2</sup>, one gets  $\xi = 0.36$  and  $\zeta = 3.83$ . The laser pulses contained about thousand cycles in a shot, allowing to neglect the details of the pulse shape and duration.

Some important difference between IPA and FPA is that in the first case the variable  $n = 1, 2, \dots$  is integer, it refers to the contribution of the individual harmonics. The value  $n\omega$  is related to the energy of the background field involved into considered quantum process. Obviously, this value is a multiple of  $\omega$ . In FPA, the basic subprocess operates with  $l$  background photons, where  $l$  is a continuous variable. The quantity  $l\omega$  can be considered as the energy partition of the laser beam involved into considered process, and it is not a multiple  $\omega$ . Mindful of this fact, without loss of generality, we denote the processes with  $l > 1$  as generalized multiphoton processes, remembering that  $l$  is a continuous quantity.

The Compton process is considered below as a spontaneous emission of one photon off an electron in an external e.m. wave. Evaluation of corresponding transition matrix is close to that of case of the Breit–Wheeler process because both processes are crossed to each other. Despite the similarities of these two processes, the physical meaning of the dynamical variables and observables is quite different. For the sake of completeness, we start our analysis from fully differential cross sections which are calculated as a function of the frequency of the outgoing photon at fixed scattering angle. The main difference to the previous studies mentioned above is utilizing a wider class of the pulse envelope functions including flat-top envelopes. However, the fully differential cross section has a complicated structure being rapidly oscillating function of the energy of the outgoing photons  $\omega'$  at fixed production angle  $\theta'$ , especially in the kinematically forbidden region. It is clear that experimental studying of the multiphoton dynamics in the case of rapidly varying cross sections is a challenging task. Rather integrated observables may overcome this problem.

But here one has to be careful. The totally integrated cross section is not suitable for this aim, because in this case the integration starts from the minimum value of the energy of the outgoing photon,  $\omega'_1$ , kinetically allowed for the electron–one-photon interaction, and this region dominates in the total cross section, masking the relatively weak effects of electron–multiphoton interactions. To highlight the role of the multiphoton interaction, the lower limit of integration  $\omega'$  must be shifted relative to  $\omega'_1$ :  $\omega' > \omega'_1$ . Such partially integrated cross sections are smooth functions of  $\omega'$  and allow one to study directly the multiphoton dynamics. Similarly to the variable  $\zeta$  in the Breit–Wheeler process, the ratio  $\kappa = \omega'/\omega'_1 > 1$  may be considered as a subthreshold variable in nonlinear Compton scattering.

We show below that in the considered quantum processes the production probability (or cross section) is determined by the nontrivial interplay of two

dynamical effects. The first one is related to the shape and duration of the pulse, while the second one is the nonlinear dynamics of the electron (positron) in the strong electromagnetic field, independently of the pulse geometry. These two effects play quite different roles in two limiting cases. The pulse shape effects manifest most clearly in the weak-field regime characterized by small values of the reduced field intensity  $\xi^2$ . The rapid variation of the e.m. field in very short (and, in particular, in subcycle) pulses enhances strongly few-photon events such that their probability may exceed the IPA result by orders of magnitude. Nonlinear multiphoton dynamics of the strong electromagnetic field plays a dominant role at large values of  $\xi^2$ . In this case, results of the IPA and the FPA are close to each other. In the transition region, i.e., at intermediate values  $\xi^2 \sim 1$ , the observables are determined by the interplay of both effects which must be taken into account simultaneously. For the quantum processes in IPA, we refer the reader to the review paper [17].

This review is based on the methods and results obtained in [25–27] and [24]. It is organized as follows. In Sec.1, we discuss the properties of envelope functions used below. Section 2 is devoted to the nonlinear Breit–Wheeler process for different pulse shapes, pulse durations and e.m. field intensities deriving the basic expressions for the probability of  $e^+e^-$  creation in FPA. We successively analyze the cases of (i) small pulse duration with number of oscillations  $N = 2–10$  at different pulse intensities, (ii) the case of large field intensity where the pulse shape becomes unessential, and (iii) subcycle pulses with  $N < 1$ , where the pulse structure is particularly important. Special attention is paid to the impact of the carrier phase. In Sec.3, we discuss several aspects of nonlinear Compton scattering for short and subcycle pulses. Our conclusions are presented in Sec.4. In Appendix, for completeness and easy reference, we present some details of a derivation of the  $e^+e^-$  production probability for very high intensities,  $\xi^2 \gg 1$ .

### 1. ENVELOPE FUNCTIONS

Below, we are going to analyze dependence of observables on the shape of  $f(\phi)$  in Eq.(1) for two types of envelopes: the one-parameter hyperbolic secant (hs) shape and the two-parameter symmetrized Fermi (sF) shape widely used for parameterization of the nuclear density [48]:

$$f_{\text{hs}}(\phi) = \frac{1}{\cosh \phi/\Delta}, \quad f_{\text{sF}}(\phi) = \frac{\cosh \Delta/b + 1}{\cosh \Delta/b + \cosh \phi/b}. \quad (8)$$

These two shapes cover a variety of relevant envelopes discussed in literature (for details, see [26]). The parameter  $b$  in the sF shape describes the ramping time in the neighborhood of  $\phi \sim \Delta$ . Small values of ratio  $b/\Delta$  cause a flat-top shaping. At  $b/\Delta \rightarrow 0$ , the sF shape becomes a rectangular pulse [18]. In the following,



we choose the ratio  $b/\Delta$  as the second independent parameter for the sF envelope function. The parameter  $\Delta$  characterizes the pulse duration  $2\Delta$  with  $\Delta = \pi N$ , where  $N$  has a meaning of a “number of oscillations” in the pulse. Certainly, such a definition is rather conditional and is especially meaningful for the flat-top envelope with small values of  $b/\Delta$ . In the case of the hs envelope shape, the number of oscillations with small amplitudes may exceed  $N$ . Nevertheless, for convenience we call  $N$  as a “number of oscillations in a pulse” for given  $f(\phi)$ , relying on its relation to the shape parameter  $\Delta$ . It was shown that the properties of the two-parameter sF shape for large values of  $b/\Delta \simeq 0.3-0.5$  are close to that of the one-parameter hs shape. Therefore, as mentioned above, in order to stress the difference between one- and two-parameter (flat-top) envelopes, we focus our consideration on the choice of  $b/\Delta = 0.15$  throughout the present paper.

The envelope shape  $f(\phi)$  and the integrand  $f^2(\phi) + f'^2(\phi)$  (which is proportional to the square of the e.m. field strength) in Eq. (6) as functions of the invariant phase for hs and sF shapes are shown in Fig. 2, *a* and 2, *b*, respectively.

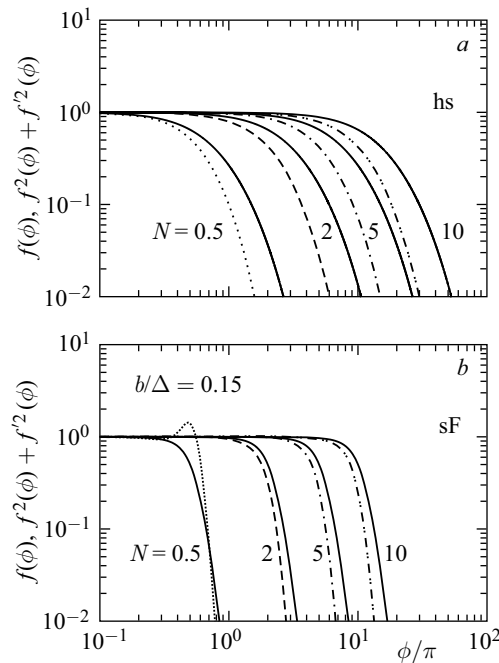


Fig. 2. The envelope functions  $f(\phi)$  and the integrand  $f^2(\phi) + f'^2(\phi)$  in Eq. (6) as the functions of the invariant phase  $\phi = kx$ . The thick solid curves labeled by  $N$  are for  $f(\phi)$ . The dotted, dashed, dash-dotted, and dot-dot-dashed curves are for  $f^2(\phi) + f'^2(\phi)$  with  $N = 0.5, 2, 5$ , and  $10$ , respectively. Panels *a* and *b* are for hs and sF envelope shapes, respectively

The numbers in the plot indicate the number of oscillations in a pulse  $N$ . The thick solid curves labeled by  $N$  are for  $f(\phi)$ . The dotted, dashed, dash-dotted and dot-dot-dashed curves are for  $f^2(\phi) + f'^2(\phi)$  with  $N = 0.5, 2, 5,$  and  $10,$  respectively. For the smooth hs shape the integrand is also a smooth function (cf. Fig. 2, *a*). For the flat-top sF envelope shape and  $N \geq 2$ , both  $f(\phi)$  and the integrand  $f^2(\phi) + f'^2(\phi)$  are smooth functions of the invariant phase which is more compact as compared with the hs shape with the same value of  $N$ . At  $N = 0.5$  and  $\phi \sim \Delta$ , the integrand (see dashed curve in the right panel) displays some overshoot resulting locally in the height  $h = 1/4 + (\Delta/b/4\Delta)^2 \simeq 1.37$ . Increasing  $\Delta$  (or  $b/\Delta$ ) leads to a vanishing of this overshoot.

For the hs envelope, the normalization factor in Eq. (6) has the form

$$N_0^{\text{hs}} = \frac{\Delta}{\pi} \left( 1 + \frac{1}{3\Delta^2} \right), \tag{9}$$

while for the sF shape the normalization factor reads

$$N_0^{\text{sF}} = \frac{\Delta}{\pi} \left( F_1(t) + F_2(t) \frac{b}{\Delta} \right), \quad t = \frac{1 + \cosh \Delta/b}{\sinh \Delta/b}, \tag{10}$$

where

$$F_1(t) = \frac{(t^2 + 1)(-t^4 + 10t^2 - 1)}{16t}, \tag{11}$$

$$F_2(t) = \frac{3t^{10} - 35t^8 + 90t^6 - 90t^4 + 35t^2 - 3}{24(t^2 - 1)^3}.$$

In the limit  $b/\Delta \rightarrow 0$ ,

$$N_0^{\text{sF}} = \frac{\Delta}{\pi} + \mathcal{O} \left( \exp \left[ -\frac{\Delta}{b} \right] \right) \simeq \frac{\Delta}{\pi}. \tag{12}$$

The normalization factor  $N_0$  scaled by  $N = \Delta/\pi$  as a function of  $N$  for hs and sF shapes is exhibited in Fig. 3, shown by the dashed and solid curves, respectively.

For the hs shape,  $N_0 \simeq N$  at  $N \geq 1$  and slightly increases for the subcycle envelopes with  $N < 1$  (cf. Eq. (9)). In the case of a flat-top envelope, the ratio  $N_0/N$  is independent of  $\Delta$ , according to Eq. (11). The contribution of  $f'^2$  in (6) is weak and varies from 0.2 to 3.8% for  $b/\Delta = 0.01$  and 0.2, respectively. In the limit  $b/\Delta \rightarrow 0$  it vanishes and  $N_0 \rightarrow N$  and, therefore, the overshoot in the integrand does not affect the integral in Eq. (6). But taking into account that very small values of  $b/\Delta$  seem to be not realistic, we restrict our actual calculations to the finite value  $b/\Delta = 0.15$ , where the overshoot in  $f^2(\phi) + f'^2(\phi)$  is minor.

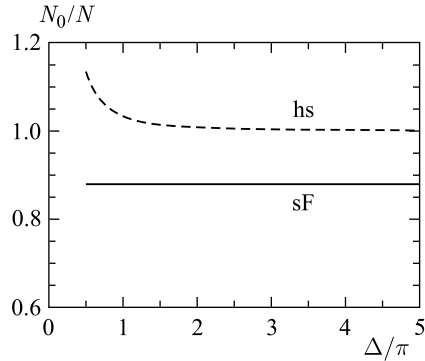


Fig. 3. The scaled normalization factor  $N_0/N$  as a function of the number of oscillations in the pulse,  $N = \Delta/\pi$ , for hs and sF shapes, shown by the dashed and solid curves, respectively

For the sake of completeness, we present also the behavior of e.m. potential  $\mathbf{A}$  and the electric field strength  $\mathbf{E} = -\partial\mathbf{A}/\partial t$ , where  $\mathbf{A}$  is given by Eqs.(1) and (8) as functions of the invariant phase  $\phi$ . The e.m. potential and strength for the one- and two-parameter envelope functions read

$$A_x = af(\phi) \cos \phi, \quad A_y = af(\phi) \sin \phi, \quad (13)$$

$$E_x = \omega A_x [-(\ln f(\phi))' + \tan \phi], \quad (14)$$

$$E_y = \omega A_y [-(\ln f(\phi))' - \cot \phi], \quad (15)$$

with  $a = |\mathbf{a}_1| = |\mathbf{a}_2|$  and

$$-(\ln f(\phi))' = \begin{cases} \frac{1}{\Delta} \tanh \frac{\phi}{\Delta}, & \text{hs,} \\ \frac{1}{b} \frac{\sinh \phi/b}{\cosh \Delta/b + \cosh \phi/b}, & \text{sF.} \end{cases} \quad (16)$$

The scaled potentials  $A_x/a$  and the scaled strengths  $E_x/a\omega$  as functions of the invariant phase are exhibited by solid and dashed curves, respectively, in upper and middle panels in Fig.4 for the hs and sF shapes. The left and right panels correspond to the pulses with  $N = 2$  and  $0.5$ , respectively. The result for the hs shape with  $N = 0.5$  is close qualitatively to that of [10]. One can see that the duration of the pulse increases with increasing number of oscillations. The flat-top sF shape is more compact compared to the hs shape with the same value of the pulse “scale” parameter  $\Delta$ .

The result for  $y$  components is exhibited in Fig.4, lower panels, where we restrict ourselves to the example of the flat-top sF envelope shape. For short pulses with  $N > 2$ , the contribution of the first terms in Eqs.(14) and (15) are relatively small and, therefore, the approximate relations  $A_y \simeq E_x/\omega$  and  $E_y \simeq -\omega A_x$  are valid. Both  $A_y$  and  $E_y$  are finite. The same is true for the sF shape with  $N \geq 2$ . This is illustrated in Fig.4, lower panel (left), where the result for the sF envelope with  $N = 2$  is shown. The approximate relations are valid also for subcycle pulse with  $N = 0.5$  and for the one-parameter hs shape. In the case of the flat-top envelope for  $N = 0.5$ , the above approximate relations are valid for  $A_y$  and for the central part of  $E_y$  (cf. Fig.4 lower panel (right)). In the border area with  $\phi \approx \Delta = \pi/2$ , the strength  $E_y$  has finite narrow peaks with height  $\tilde{h} =$

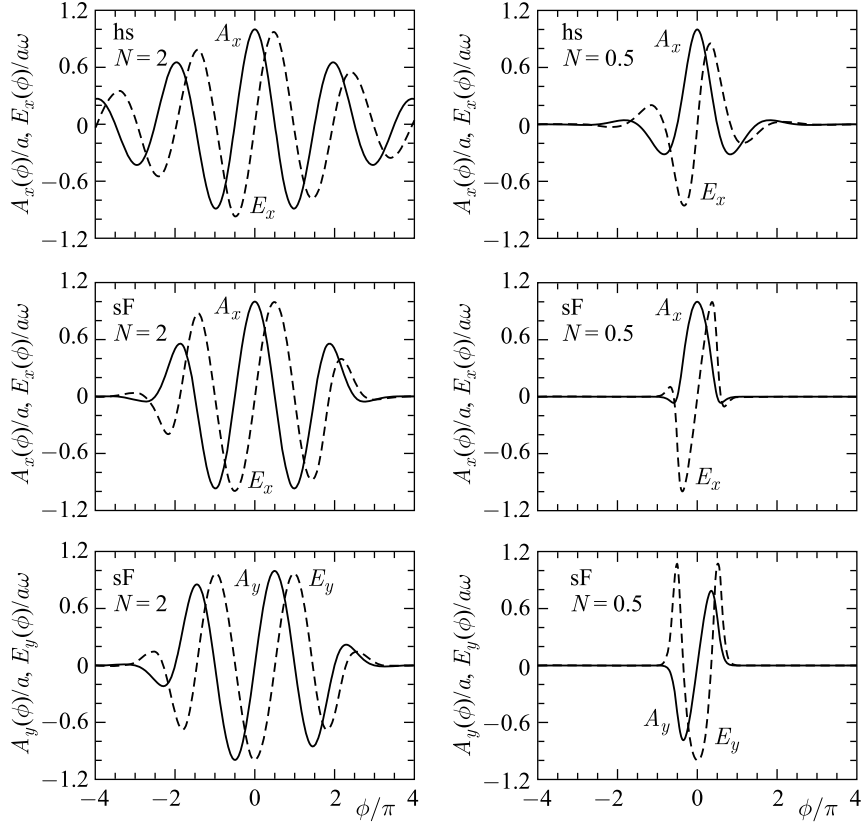


Fig. 4. The e.m. potentials  $A/a$  (solid curves) and field strengths  $E/a\omega$  (dashed curves) as functions of the invariant phase  $\phi$ . The upper and middle panels correspond to the hyperbolic secant (hs) and symmetrized Fermi (sF) shapes, respectively, for the  $x$  components. The lower panels correspond to the  $y$  components for the sF envelope shape. The left and right panels are for pulses with  $N = 2$  and  $N = 0.5$ , respectively

$\left(\frac{\Delta}{b}\right) \frac{\sin \Delta}{4\Delta} + \mathcal{O}(\exp(-\Delta/b)) \simeq 1.06$ . The height of these peaks decreases with increasing  $\Delta$  at fixed  $b/\Delta$  and for  $N \geq 2$  it becomes negligibly small. This “pick-like” behavior for the flat-top shape can be compared with the popular rectangular pulse [18], where the derivative  $f'(\phi) = \theta'(\phi - \Delta) = \delta(\phi - \Delta)$  is singular at  $\phi = \Delta$ . But such a “pick-like” or even singular behavior of  $\mathbf{E}$  at the border does not affect the transition matrix elements, discussed in the next section (cf. Eq. (18)), since they are determined by  $\mathbf{A}$  and  $\mathbf{A}^2$  rather than the e.m. strength.

Therefore, our plots and discussions for the e.m. strength  $E_{x,y}$  have an illustrative character since the dynamics of the considered process is determined purely by the e.m. potential  $A_{x,y}$ , which is taken, in our approach, as a primary quantity.

## 2. THE $e^+e^-$ PAIR PRODUCTION IN A FINITE PULSE

**2.1. General Formalism.** In our consideration of quantum processes, we start from  $e^+e^-$  pair production in the interaction of a probe photon with a circularly polarized e.m. field described by Eq.(1). Within the Furry picture, the process is diagrammatically represented by the one-vertex graph, describing the decay of the probe photon with the four-momentum  $k'$  into a laser dressed  $e^+e^-$  pair, where the presence of the background e.m. field is included in the Volkov solution of the outgoing  $e^+$  and  $e^-$ . (In the weak-field approximation this graph turns into the known two two-vertex graphs for the perturbative Breit–Wheeler process.) Utilization of (1) leads to two significant modifications of the transition amplitude in FPA compared to IPA. In IPA, the Volkov solutions [49, 50] refer to fermions with quasi-momenta  $q_\mu = p_\mu + k_\mu \frac{\xi^2 m^2}{2(k \cdot p)}$  and dressed masses  $m_*^2 = m^2(1 + \xi^2)$ . In FPA, all fermion momenta and masses take their vacuum values  $p$  and  $m$ , respectively, whereas the corresponding wave functions are modified in accordance with the Volkov solution (with more complicated, compare to IPA, phase factor). The finite (in space-time) e.m. potential (1) for FPA requires the use of Fourier integrals for invariant amplitudes, instead of Fourier series which are employed in IPA. The partial harmonics become thus continuously in FPA. The  $S$ -matrix element is expressed generically as

$$S_{fi} = \frac{-ie}{\sqrt{2p_0 2p'_0 2\omega'}} \int_{\zeta}^{\infty} dl M_{fi}(l) (2\pi)^4 \delta^4(k' + lk - p - p'), \quad (17)$$

where  $k$ ,  $k'$ ,  $p$ , and  $p'$  refer to the four-momenta of the background (laser) field (1), incoming probe photon, outgoing positron and electron, respectively, the low limit  $\zeta$  is defined in Eq. (7). The transition matrix  $M_{fi}(l)$  consists of four terms

$$M_{fi}(l) = \sum_{i=0}^3 M^{(i)} C^{(i)}(l), \quad (18)$$

where

$$\begin{aligned}
 C^{(0)}(l) &= \frac{1}{2\pi} \int_{-\infty}^{\infty} d\phi e^{il\phi - i\mathcal{P}(\phi)}, \\
 C^{(1)}(l) &= \frac{1}{2\pi} \int_{-\infty}^{\infty} d\phi f^2(\phi) e^{il\phi - i\mathcal{P}(\phi)}, \\
 C^{(2)}(l) &= \frac{1}{2\pi} \int_{-\infty}^{\infty} d\phi f(\phi) \cos \phi e^{il\phi - i\mathcal{P}(\phi)}, \\
 C^{(3)}(l) &= \frac{1}{2\pi} \int_{-\infty}^{\infty} d\phi f(\phi) \sin \phi e^{il\phi - i\mathcal{P}(\phi)},
 \end{aligned} \tag{19}$$

with

$$\mathcal{P}(\phi) = z \int_{-\infty}^{\phi} d\phi' \cos(\phi' - \phi_0) f(\phi') - \xi^2 \zeta u \int_{-\infty}^{\phi} d\phi' f^2(\phi'). \tag{20}$$

The quantity  $z$  is related to  $\xi$ ,  $l$ , and  $u \equiv (k' \cdot k)^2 / (4(k \cdot p)(k \cdot p'))$  via

$$z = 2l\xi \sqrt{\frac{u}{u_l} \left(1 - \frac{u}{u_l}\right)}, \tag{21}$$

with  $u_l \equiv l/\zeta$ . The phase  $\phi_0$  is equal to the azimuthal angle of the direction of flight of the outgoing electron in the  $e^+e^-$  pair rest frame  $\phi_0 = \phi_{p'} \equiv \phi_e$  and it is related to the azimuthal angle of the positron momentum as  $\phi_0 = \phi_{e^+} + \pi$ . Similarly to IPA, it can be determined through invariants  $\alpha_{1,2}$  as  $\cos \phi_0 = \alpha_1/z$ ,  $\sin \phi_0 = \alpha_2/z$  with  $\alpha_{1,2} = e(a_{1,2} \cdot p/k \cdot p - a_{1,2} \cdot p'/k \cdot p')$ .

The transition operators  $M^{(i)}$  in Eq. (18) have the form

$$M^{(i)} = \bar{u}_{p'} \hat{M}^{(i)} v_p, \tag{22}$$

with

$$\begin{aligned}
 \hat{M}^{(0)} &= \not{\epsilon}', \\
 \hat{M}^{(1)} &= -\frac{e^2 a^2 (\epsilon' \cdot k) \not{k}}{2(k \cdot p)(k \cdot p')}, \\
 \hat{M}^{(2,3)} &= \frac{e \not{\phi}_{(1,2)} \not{k} \not{\epsilon}'}{2(k \cdot p')} - \frac{e \not{\epsilon}' \not{k} \not{\phi}_{(1,2)}}{2(k \cdot p)},
 \end{aligned} \tag{23}$$

where  $u_{p'}$  and  $v_p$  are the Dirac spinors of the electron and positron, respectively, and  $\varepsilon'$  is the polarization four-vector of the probe photon.

The integrand of the function  $C^{(0)}$  in Eqs. (19) does not contain the envelope function  $f(\phi)$  and therefore it is divergent. One can regularize it by using the prescription of [18] which leads to

$$C^{(0)}(l) = \frac{1}{2\pi l} \int_{-\infty}^{\infty} d\phi (z \cos(\phi - \phi_0) f(\phi) - \xi^2 \zeta u f^2(\phi)) \times \\ \times e^{il\phi - i\mathcal{P}(\phi)} + \delta(l) e^{-i\mathcal{P}(0)}. \quad (24)$$

This expression contains a singular (last) term which, however, does not contribute because of kinematical restriction, implying  $l > 0$ .

The differential probability of  $e^+e^-$  pair production in terms of the transition matrix  $M_{fi}(l)$  in Eq. (17) reads

$$dW = \frac{\alpha \zeta^{1/2}}{2\pi N_0 m} \int_{\zeta}^{\infty} dl |M_{fi}(l)|^2 \frac{d\mathbf{p}}{2p_0} \frac{d\mathbf{p}'}{2p'_0} \delta^4(k' + lk - p - p'). \quad (25)$$

It may be represented in a conventional form as a function of  $u$  and  $\phi_e$ ,

$$\frac{dW}{d\phi_e du} = \frac{\alpha m \zeta^{1/2}}{16\pi N_0} \frac{1}{u^{3/2} \sqrt{u-1}} \int_{\zeta}^{\infty} dl w(l), \quad (26)$$

with

$$\frac{1}{2} w(l) = (2ul + 1) |C^{(0)}(l)|^2 + \xi^2 (2u - 1) (|C^{(2)}(l)|^2 + |C^{(3)}(l)|^2) + \\ + \text{Re } C^{(0)}(l) \left( \xi^2 C^{(1)}(l) - \frac{2z}{\zeta} (\cos \phi_0 C^{(2)}(l) + \sin \phi_0 C^{(3)}(l)) \right)^*. \quad (27)$$

The normalization factor  $N_0$  is determined by Eq. (6) and has been discussed in the previous section.

It is convenient to express the  $C^{(i)}(l)$  functions defined in Eqs. (19) and (24) through the new, basic functions  $Y_l$  and  $X_l$ , which may be considered as an analog of the Bessel functions in IPA,

$$Y_l(z) = \frac{1}{2\pi} e^{-il\phi_0} \int_{-\infty}^{\infty} d\phi f(\phi) e^{il\phi - i\mathcal{P}(\phi)}, \\ X_l(z) = \frac{1}{2\pi} e^{-il\phi_0} \int_{-\infty}^{\infty} d\phi f^2(\phi) e^{il\phi - i\mathcal{P}(\phi)}. \quad (28)$$

The new representation of the basic functions  $C^{(i)}(l)$  reads

$$\begin{aligned}
 C^{(1)}(l) &= X_l(z) e^{il\phi_0}, \\
 C^{(2)}(l) &= \frac{1}{2} \left( Y_{l+1} e^{i(l+1)\phi_0} + Y_{l-1} e^{i(l-1)\phi_0} \right), \\
 C^{(3)}(l) &= \frac{1}{2i} \left( Y_{l+1} e^{i(l+1)\phi_0} - Y_{l-1} e^{i(l-1)\phi_0} \right), \\
 C^{(0)}(l) &= \tilde{Y}_l(z) e^{il\phi_0}, \\
 \tilde{Y}_l(z) &= \frac{z}{2l} (Y_{l+1}(z) + Y_{l-1}(z)) - \xi^2 \frac{u}{u_l} X_l(z).
 \end{aligned}
 \tag{29}$$

It allows one to express  $w(l)$  in Eq.(27) in the form

$$w(l) = 2\tilde{Y}_l^2(z) + \xi^2(2u - 1) \left( Y_{l-1}^2(z) + Y_{l+1}^2(z) - 2\tilde{Y}_l(z)X_l^*(z) \right), \tag{30}$$

which resembles the expression for the probability in the case of IPA

$$w_n = 2J_n^2(z) + \xi^2(2u - 1) \left( J_{n-1}^2(z) + J_{n+1}^2(z) - 2J_n^2(z) \right), \tag{31}$$

with the substitution  $\tilde{Y}_l^2(z) \rightarrow J_n^2(z)$ ,  $Y_{l\pm 1}^2(z) \rightarrow J_{n\pm 1}^2(z)$ , and  $\tilde{Y}_l(z)X_l^*(z) \rightarrow J_n^2(z)$ .

The differential probability  $dW$  in Eq.(26) is, in fact, the probability per unit time (or rate), and it is related to the differential cross section  $d\sigma$  as

$$dW = J\rho_\gamma d\sigma = 2\frac{\omega m^2 \xi^2}{4\pi\alpha} d\sigma, \tag{32}$$

where  $J = 2$  and  $\rho_\gamma$  are the flux of incoming probe photon and the density of the background photons, respectively,  $\omega$  is the frequency of the background photon. Thus, the differential cross section reads

$$\frac{d\sigma}{d\phi_p du} = \frac{\alpha^2 \zeta}{2s_{\text{thr}} \xi^2 N_0} \frac{1}{u^{3/2} \sqrt{u-1}} \int_{\zeta}^{\infty} dl w(l). \tag{33}$$

Later, for easy reference and comparison with the previous works (cf. [17]), we present our results for the Breit–Wheeler process in terms of probabilities  $dW$  (production rates) rather than the cross sections  $d\sigma$ , remembering Eq.(32) connecting these two observables.

**2.2. Short Pulses.** In this section, we consider short pulses with the number of oscillation  $N \geq 2$ , however, the developed methods for studying probabilities of  $e^+e^-$  pair production are valid even for pulses with  $N \sim 1$ . The subcycle pulses with  $N < 1$  will be considered separately. Recall that we consider two



envelope shapes: hyperbolic secant (hs) shape and symmetrized Fermi (sF) shape with  $b/\Delta = 0.15$ .

As mentioned above, Eqs. (26) and (33) with Eq. (27) can be used for numerical estimates of the  $e^+e^-$  production probability or cross section evaluating five-dimensional integral(s) with rapidly oscillating functions. Technically, such an approach needs long calculation time for reasonable computational accuracy which makes it difficult for applications in transport/Monte Carlo codes. However, a closer inspection of the functions  $\mathcal{P}(\phi)$  and  $Y_l, X_l$  shows that the number of integrations may be reduced and, in some cases, Eq. (30) may be expressed in an analytical form. Thus, integrating by parts the function  $\mathcal{P}(\phi)$  might be rewritten in the following form:

$$\mathcal{P}(\phi) \equiv \mathcal{P}_0(\phi) - \xi^2 \zeta u \int_{-\infty}^{\phi} d\phi' f^2(\phi'), \quad (34)$$

$$\mathcal{P}_0(\phi) = z \left( \sin(\phi - \phi_0) f(\phi) + \mathcal{O}\left(\frac{1}{\Delta}\right) \right),$$

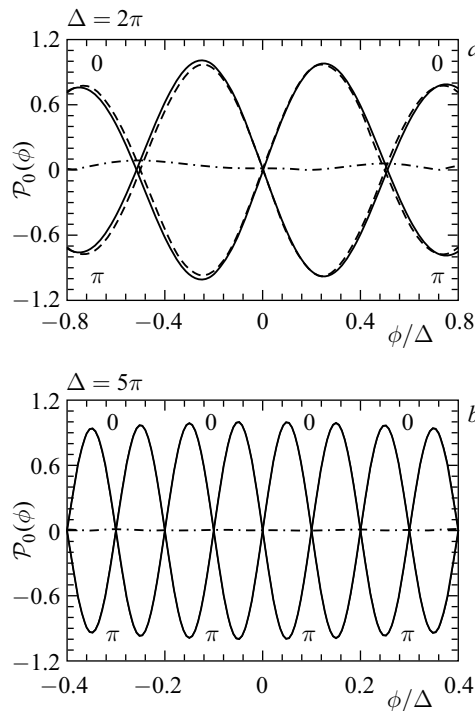


Fig. 5. The function  $\mathcal{P}_0(\phi)$  defined in (34) with (solid curves) and without (dashed curves) the term (35) for  $\Delta = \pi N$  with  $N = 2$  and  $5$ , shown in panels *a* and *b*, respectively. The term (35) is shown separately by dash-dotted curves

with

$$\mathcal{O}\left(\frac{1}{\Delta}\right) = -\frac{1}{\Delta} \int_{-\infty}^{\phi} d\phi' \sin(\phi' - \phi_0) f'(\phi'). \tag{35}$$

The contribution of this term to  $\mathcal{P}(\phi)$  is subleading for the finite pulse size  $\Delta = \pi N$  with  $N \geq 2$ . First, because of the explicit factor  $1/\Delta$ , and second, because the derivative  $f'(\phi)$  in the integrand reaches its maximum value at the boundaries of the pulse, where this function is suppressed. For an illustration, in Fig. 5 we present results of a numerical analysis of  $\mathcal{P}_0(\phi)$  with the hyperbolic secant envelope function. The solid and dashed curves exhibit calculations with and without the term (35), respectively, for  $\phi_0 = 0$  and  $\pi$ . The left and right panels correspond to  $\Delta = \pi N$  with  $N = 2$  and  $5$ , respectively. The term  $(|\mathcal{O}(1/\Delta)|)$  is shown by dash-dotted curves. One can see, in fact, that this term is rather small and may be omitted. The second term in expression for  $\mathcal{P}(\phi)$  in Eq. (34) is a smooth function of  $\phi$  and in case of hs shape it can be given explicitly as  $-\xi^2 \zeta u \Delta \tanh(\phi/\Delta)$ .

Now we are going to discuss separately the weak-, intermediate- and strong-field regimes.

**2.3. Pair Production at Small Field Intensities ( $\xi^2 \ll 1$ ).** In case of small  $\xi^2 \ll 1$ , implying  $z < 1$ , we decompose  $l = n + \epsilon$ , where  $n$  is the integer part of  $l$ , yielding

$$\begin{aligned} Y_l &\simeq \frac{1}{2\pi} \int_{-\infty}^{\infty} d\psi e^{i l \psi - i z \sin \psi} f(\psi + \phi_0) f(\psi + \phi_0), \\ &= \frac{1}{2\pi} \int_{-\infty}^{\infty} d\psi \sum_{m=0}^{\infty} \frac{(iz)^m}{m!} \sin^m \psi e^{i(n+\epsilon)\psi} f^{m+1}(\psi + \phi_0). \end{aligned} \tag{36}$$

Similarly, for the function  $X_l(z)$  the substitution  $f^{m+1} \rightarrow f^{m+2}$  applies. The dominant contribution to the integral in (36) with rapidly oscillating integrand comes from the term with  $m = n$ , which results in

$$Y_{n+\epsilon} \simeq \frac{z^n}{2^n n!} e^{-i\epsilon\phi_0} F^{(n+1)}(\epsilon), \quad X_{n+\epsilon} \simeq \frac{z^n}{2^n n!} e^{-i\epsilon\phi_0} F^{(n+2)}(\epsilon), \tag{37}$$

where the function  $F^{(n)}(\epsilon)$  is the Fourier transform of the function  $f^n(\psi)$ .

As an example, let us analyze the  $e^+e^-$  production near the threshold, i.e.,  $\zeta \sim 1$ . In this case, the contribution with  $n = 1$  is dominant and, therefore, the functions  $Y_{0+\epsilon}$  are crucial, including the first term in (30). The functions  $X_{0+\epsilon}$  are not important because they are multiplied by the small  $\xi^2$  and may be omitted. Negative  $\epsilon = \zeta - 1$  and positive  $\epsilon$  correspond to the above- and subthreshold pair

production, respectively. The function  $Y_{0+\epsilon}$  reads  $Y_{0+\epsilon} = F^{(1)}(\epsilon) \exp[-i\phi_0\epsilon]$ , where the Fourier transforms  $F^{(1)}(x)$  for the hs and sF envelope functions are equal to

$$\begin{aligned} F_{\text{hs}}(x) &= \frac{\Delta}{2 \cosh \frac{1}{2} \pi \Delta x}, \\ F_{\text{sF}}(x) &= \frac{1 + \exp[-\Delta/b]}{1 - \exp[-\Delta/b]} \frac{b \sin \Delta l}{\sinh \pi b x}. \end{aligned} \quad (38)$$

The  $\phi_0$  dependence of the production probability disappears in this case because the latter one is determined by the quadratic terms of the  $Y$  functions.

Consider first the pair production above the threshold. Keeping the terms with leading power of  $\xi^2$  one can express the production probability as

$$\frac{dW}{du} = \frac{\alpha M_e \zeta^{1/2}}{4N_0} \left[ \frac{u}{u_1} \left( 1 - \frac{u}{u_1} \right) + u - \frac{1}{2} \right] \frac{\xi^2}{u^{3/2} \sqrt{(u-1)}} I_0, \quad (39)$$

where, taking into account that, at finite values of  $\Delta$ , Fourier transforms for all considered envelopes decrease rapidly with increasing  $\epsilon$ , one can get

$$I_0 \simeq \int_{1-\zeta}^{1/2} d\epsilon F^{(1)2}(\epsilon) \simeq \int_{-\infty}^{\infty} d\epsilon F^{(1)2}(\epsilon) = \frac{1}{2\pi} \int_{-\infty}^{\infty} d\phi f^2(\phi) \simeq N_0. \quad (40)$$

Combining these two equations one recovers the IPA result [17]. Thus, we can conclude that for small field intensities for a finite pulse duration, the probabilities of  $e^+e^-$  pair emission above threshold with  $\zeta < 1$  in IPA and FPA coincide, independently of the shape of the envelope function. For an illustration, in Fig. 6 we show the partial probability  $w(l)$ , calculated at  $u = 1$  for the above-threshold region with  $\xi = 10^{-2}$  and  $\zeta = 0.5$  in a finite region of  $l$  for the envelope size  $\Delta = \pi N$  with  $N = 2$  and 10, respectively. For the envelope with a hyperbolic secant shape (Fig. 6, *a*) one can see smooth curves with maxima at integer values of  $l$ . The widths of bumps decrease with increasing  $N$ . However, the integral of  $w(l)$  over  $l$  in the neighborhood of the first maximum is independent of  $N$  and coincides with the contribution of the first harmonic in IPA which leads to an equality of IPA and FPA results. For the symmetrized Fermi shape (Fig. 6, *b*) the situation is different in some sense. The corresponding Fourier transforms  $F_{\text{sF}}^{(n)}(l)$  in (37) oscillate with  $l$ . For example, the function  $F_{\text{sF}}^{(1)}$  goes to zero at a multiple of  $1/N$ . This results in an oscillating structure of  $w(l)$ . However, the exponential decrease of  $w(l)$  with increasing of the integer values of  $l$  is the same.

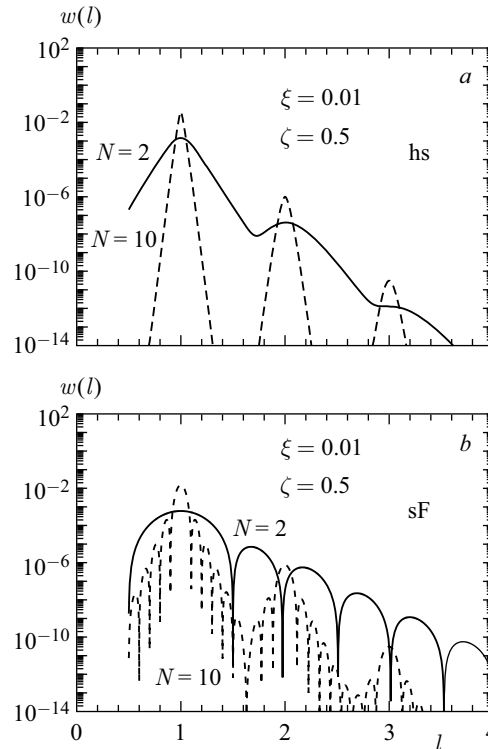


Fig. 6. The partial probability  $w(l)$  defined in (30) as a function of  $l$  at  $u = 1$ . The solid and dashed curves correspond to the parameter  $\Delta = \pi N$  with  $N = 2$  and  $10$ , respectively. Panels *a* and *b* exhibit results for the envelopes with hyperbolic secant and symmetrized Fermi shapes, respectively, for  $\xi^2 = 10^{-4}$  and  $\zeta = 0.5$

The situation changes when we are slightly below threshold, i.e.,  $\zeta > 1$ . In this case, the function  $Y_{0+\epsilon}$  dominates again and the result for FPA is the same as in (39) but with the substitution  $I_0 \rightarrow I_1$ , with  $I_1 \simeq \int_{\zeta-1}^1 d\epsilon F^{(1)2}(\epsilon)$ . In the case of smooth envelope shape (e.g., hyperbolic secant) the dominating contribution to this integral comes from the lower limit and, therefore,  $I_1 \sim (F_{\text{hs}}^{(1)}(\zeta - 1))^2$ . As a result, the production probability strongly depends on the duration  $\Delta$  of the pulse. In the case of a flat-top envelope, we have a similar effect, because  $F_{\text{sF}}^{(1)}(l)$ , in general, decreases exponentially as  $\exp(-\pi bl)$ , where  $b$  increases with increasing  $N$  at fixed  $b/\Delta$ .

In Fig. 7, we show the partial probability  $w(l)$  in the subthreshold region with  $\zeta = 1.25$ . One can see that for the hyperbolic secant envelope (Fig. 7, *a*) the

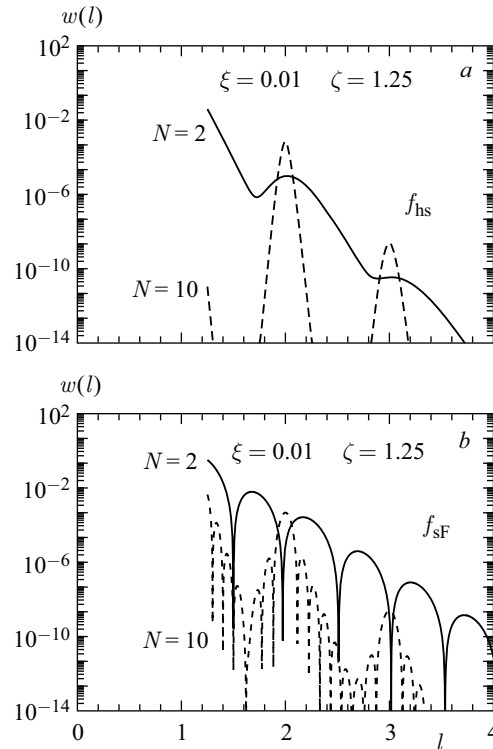


Fig. 7. The same as in Fig. 6, but for the subthreshold region at  $\zeta = 1.25$

difference of  $w(l)$  at  $l \simeq \zeta$  for  $N = 2$  and  $N = 10$  is more than several orders of magnitude, which will be reflected in the total probability. In the case of the symmetrized Fermi envelope shape, one also can see a significant enhancement of  $w(l)$  for  $N = 2$  compared to  $N = 10$ . But now, the difference between FPA and IPA is larger compared to the case of the hyperbolic secant shape.

The total probability  $W$  of  $e^+e^-$  emission as a function of the subthreshold parameter  $\zeta$  in the vicinity  $\zeta \sim 1$  is presented in Fig. 8. The dashed and solid curves correspond to the hyperbolic secant and symmetrized Fermi envelope shapes, respectively. Figure 8, *a* and *b* correspond to the short pulses with  $\Delta = \pi N$  for  $N = 2$  and 10, respectively, at  $\xi^2 = 10^{-4}$ . For comparison, we present also the IPA results. In the above-threshold region, results of IPA and FPA are equal to each other according to Eqs. (39) and (40). However, in the subthreshold region, where  $\zeta$  is close to unity, the probability of FPA considerably exceeds (by more than two orders of magnitude) the corresponding IPA result. In the case of the hyperbolic secant envelope function, the probability increases with

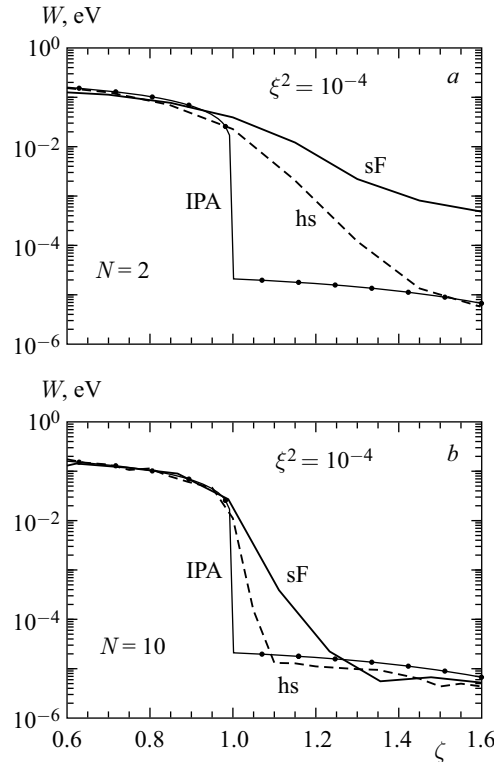


Fig. 8. The total probability  $W$  of the  $e^+e^-$  pair production as a function of  $\zeta$  for short pulses with  $\Delta = \pi N$  for  $N = 2$  and  $10$  is shown in panels  $a$  and  $b$ , respectively;  $\xi^2 = 10^{-4}$ . The dashed and solid curves correspond to the hyperbolic secant and symmetrized Fermi envelope shapes, respectively. The thin solid curves marked by dots depict the IPA result

decreasing pulse duration. The results of FPA and IPA become comparable at  $N \geq 10$ . Qualitatively, this result is also valid for the case of the symmetrized Fermi distribution. However, in this case the enhancement of the probability in FPA is much greater. This is due to the fact that the maxima in the partial probability  $w(l)$  (cf. Fig. 7) decreases with increasing  $l$  in different ways for different envelope shapes. In the case of the hyperbolic secant, it decreases as  $\exp(-\pi\Delta l)$ , whereas in the case of symmetrized Fermi shape it decreases as  $\exp(-2\pi b l)$ . For the latter one, at  $b/\Delta = 0.15$  the slope is much smaller. Such a strong gain of  $e^+e^-$  emission rate is expected for other values of  $\zeta$ , when  $\zeta$  exceeds an integer number. This effect is illustrated in Figs. 9 and 10, where the total  $e^+e^-$  production probability  $W$  is presented in a wide region of  $\zeta$  at  $\xi^2 = 10^{-4}$ .

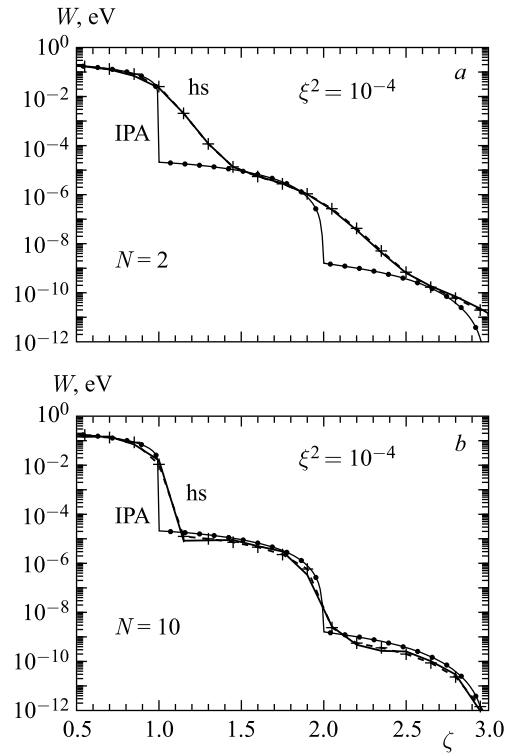


Fig. 9. The total probability  $W$  of the  $e^+e^-$  pair production as a function of  $\zeta$  for the hyperbolic secant envelope shape. The solid curves are for the full calculation, while the dashed curves marked by crosses correspond to the approximate result with the basic functions taken in the form of Eq. (37). Panels *a* and *b* correspond to the number of oscillation in a pulse  $N = 2$  and 10, respectively;  $\xi^2 = 10^{-4}$

In Fig. 9, we present the results for the hyperbolic secant envelope shape. The solid curves are for the full calculation, while the dashed curves marked by crosses correspond to the approximate result with the basic functions taken in the form of Eq. (37). Figure 9, *a* and *b* corresponds to the number of oscillation in a pulse  $N = 2$  and 10, respectively. One can see that the approximate result is in very good agreement with the full calculation and may be used in transport code calculations since it is much easier acceptable.

Corresponding results for the symmetrized Fermi shape envelopes are shown in Fig. 10. In the case of short pulse with  $N = 2$ , the approximate calculation is valid at  $\zeta \lesssim 1.7$ . However, when  $N$  increases, one can find agreement between full and approximate results in a wide region of  $\zeta$ . For the flat-top shape with

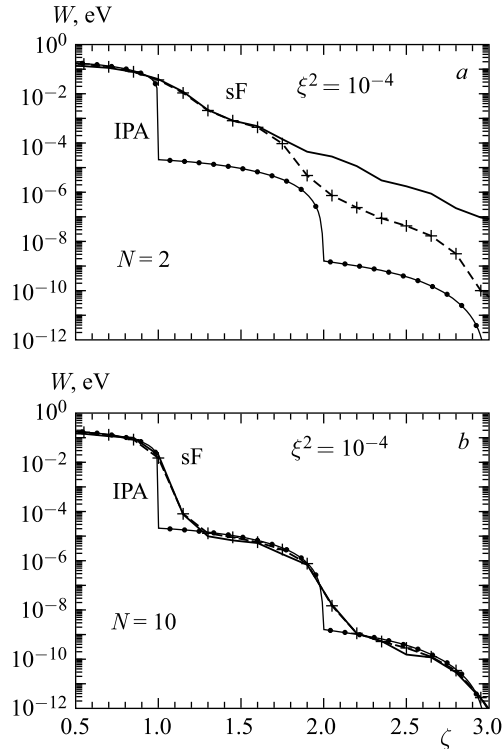


Fig. 10. The same as in Fig. 9, but for symmetrized Fermi shape

small  $b/\Delta$ , the probability in FPA is larger than the result of IPA near integer values of  $\zeta$ .

In any case, at large values of  $N$  (Fig. 10,  $b$ ,  $N = 10$ ) results of FPA and IPA become close to each other, especially for the one-parameter envelope shapes. For this case, at least for  $\xi = 0.1, \dots, 0.01$ ,  $N \simeq 10$  can be considered to be near by infinite, when considering the overall  $\zeta$  dependence.

To summarize this part, we would like to note that temporal beam shape effects for short pulses are strong and even dominant at small field intensities in the parameter region where the variable  $z$  is small,  $z < 1$ . At finite  $z$ , the nonlinear dynamics of  $e^+e^-$  production at high pulse intensity becomes essential.

**2.4. The Case of Intermediate Field Intensity ( $\xi^2 \sim 1$ ).** At finite values of  $z$ ,  $z \gtrsim 1$ , the probability of  $e^+e^-$  emission needs to be calculated numerically using Eqs. (26), (30), and (28). In Fig. 11, we present the total probability  $W$  as a function of  $\zeta$  at fixed  $\xi^2 = 1$  (plot  $a$ ) and as a function of  $\xi^2$  at fixed  $\zeta = 4$  (plot  $b$ ). The calculations are performed for the hyperbolic secant and symmetrized Fermi



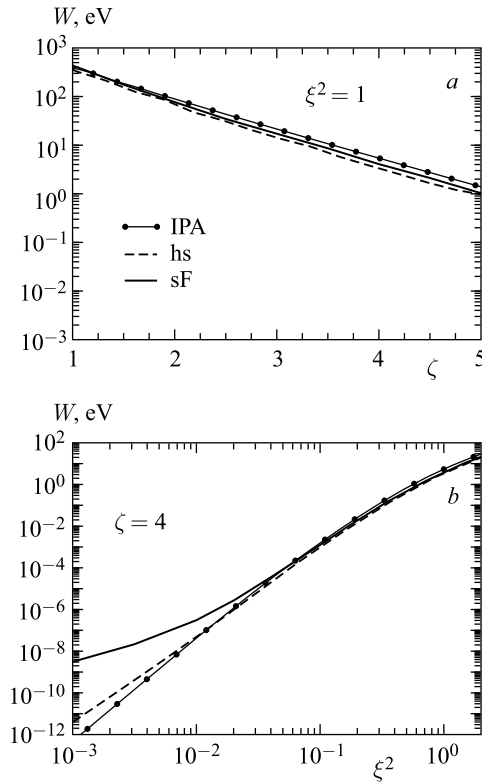


Fig. 11. The total probability of  $e^+e^-$  pair production for two envelope shapes (dashed and solid curves are for hyperbolic secant and symmetrized Fermi shapes, respectively). The thin solid curves marked by dots are the result of IPA. *a*) The total probability as a function of  $\zeta$  at  $\xi^2 = 1$ . *b*) The total probability as a function of  $\xi^2$  at  $\zeta = 4$

pulse envelope shapes, shown by the dashed and solid curves, respectively. The duration of the pulse is  $\Delta = \pi N$  with  $N = 2$ . For comparison, we also present IPA results by the thin solid curves marked by dots. At finite  $\xi^2$ , the probability decreases monotonically with increasing  $\zeta$  (Fig. 11, *a*), contrary to the step-like decrease typical for the small  $\xi^2 \ll 1$  (cf. Figs. 9, *b* and 10, *b*).

Concerning the  $\xi^2$  dependence (Fig. 11, *b*), one can see a sizeable enhancement of the total probability  $W$  at small values of  $\xi^2$  for the flat-top pulse shape compared to the case of hyperbolic secant and the IPA result. The latter two results are practically identical to each other. At  $\xi^2 \geq 0.1$ , the production probability does not sensitively depend on the pulse shape, and FPA and IPA results are close to each other. This means that at large field intensity,

the dynamical aspects of the pair production gain a dominant role in comparison with the pulse shape and size effects.

Finally, we note that, at finite  $\xi^2$ , the dependence of the probability on the azimuthal angle  $\phi_e$  disappears and the distribution in the  $x-y$  plane becomes isotropic.

As an example, in Fig. 12 we present prediction for the differential probability of  $e^+e^-$  pair production as a function of  $\phi_e = \phi_0$  at  $\zeta = 4$  for the hyperbolic secant pulse shape with  $N = 2$  at  $\xi^2 = 0.1, 1, \text{ and } 10$ . This result reflects the isotropy of the  $e^+e^-$  emission and exposes the  $\xi^2$  dependence in the considered kinematical region.

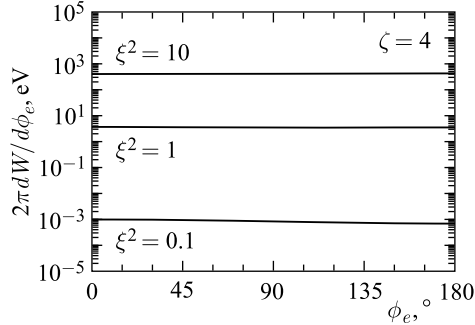


Fig. 12. The differential probability of  $e^+e^-$  pair production as a function of  $\phi_{e'} = \phi_0$  at  $\zeta = 4$  and  $N = 2$  for different values of  $\xi^2$

**2.5. Pair Production at Large Field Intensity ( $\xi^2 \gg 1$ ).** At large values of  $\xi^2 \gg 1$ , the basic functions  $Y_l$  and  $X_l$  in Eq. (28) can be expressed in the form of (49):

$$Y_l = \int_{-\infty}^{\infty} dq F^{(1)}(q) G(l - q), \quad X_l = \int_{-\infty}^{\infty} dq F^{(2)}(q) G(l - q), \quad (41)$$

where  $F^{(1)}(q)$  and  $F^{(2)}(q)$  are Fourier transforms of the functions  $f(\phi)$  and  $f^2(\phi)$ , respectively, and  $G(l)$  may be written as

$$G(l) = \frac{1}{2\pi} \int_{-\infty}^{\infty} d\phi e^{i(l\phi - z \sin \phi + \xi^2 \zeta u \phi)}. \quad (42)$$

In deriving this equation we have considered the following facts: (i) at large  $\xi^2$  the probability is isotropic, therefore we put  $\phi_0 = 0$ , (ii) the dominant contribution to the rapidly oscillating exponent comes from the region  $\phi \simeq 0$ , where the difference of two large values  $l\phi$  and  $z \sin \phi$  is minimal, and therefore, one can decompose the last term in the function  $\mathcal{P}(\phi)$  in (34) around  $\phi = 0$ , and (iii) replace in exponent  $f(\phi)$  by  $f(0) = 1$ .

Equation (42) represents an asymptotic form of the Bessel functions  $J_{\tilde{l}}(z)$  [51] with  $\tilde{l} = l + \xi^2 \zeta u$  at  $\tilde{l} \gg 1$ ,  $z \gg 1$ , and therefore the following identities are valid:

$$G(\tilde{l} - 1) - G(\tilde{l} + 1) = 2G'_z(\tilde{l}), \quad G(\tilde{l} - 1) + G(\tilde{l} + 1) = 2\frac{\tilde{l}}{z}G(\tilde{l}), \quad (43)$$

which allow one to express the partial probability  $w(\tilde{l})$  in (30) as a sum of the diagonal (relative to  $\tilde{l}$ ) terms:  $Y_{\tilde{l}}^2$ ,  $Y_{\tilde{l}}X_{\tilde{l}}$ ,  $X_{\tilde{l}}^2$  and  $Y_{\tilde{l}}'^2$ . The integral over  $\tilde{l}$  from

the diagonal term can be expressed as

$$I_{YY} = \int_{\tilde{l}_0}^{\infty} d\tilde{l} Y_{\tilde{l}}^2 = \int dq dq' F^{(1)}(q) F^{(1)}(q') \int_{\tilde{l}_0}^{\infty} d\tilde{l} G(\tilde{l} - q) G(\tilde{l} - q'), \quad (44)$$

where  $\tilde{l}_0 = \zeta(1 + \xi^2 u)$ . Taking into account that for the rapidly oscillating  $G$  functions  $G(l - q)G(l - q') \simeq \delta(q - q')G^2(l - q)$  and  $\langle q \rangle \ll \langle l \rangle \sim \xi^2$ , one gets

$$I_{YY} = \frac{1}{2\pi} \int_{-\infty}^{\infty} d\phi f^2(\phi) \int_{\tilde{l}_0}^{\infty} d\tilde{l} G^2(\tilde{l}) = N_{YY} \int_{\tilde{l}_0}^{\infty} d\tilde{l} G^2(\tilde{l}). \quad (45)$$

Similar expressions are valid for the other diagonal terms with own normalization factors. For the  $X_{\tilde{l}}^2$  term it is  $N_{XX} = (1/2\pi) \int_{-\infty}^{\infty} d\phi f^4(\phi)$ ; and for  $Y_{\tilde{l}}X_{\tilde{l}}$ ,  $N_{YX} = (1/2\pi) \int_{-\infty}^{\infty} d\phi f^3(\phi)$ . At large  $\xi^2$ , the probability does not depend on the envelope shape, because only the central part of the envelope is important. Therefore, for simplicity, we choose the flat-top shape with  $N_{YY} = N_{YX} = N_{XX} = N_0 = \Delta/\pi$  which is valid for any smooth (at  $\phi \simeq 0$ ) envelopes.

Making a change of the variable  $l \rightarrow \tilde{l} = l + \xi^2 \zeta u$ , the variable  $z$  takes the following form:

$$z^2 = 4\xi^2 \zeta^2 (uu_l - u^2) = \frac{4\xi^2 l_0^2}{1 + \xi^2} (uu_{\tilde{l}} - u^2), \quad (46)$$

with  $l_0 = \zeta(1 + \xi^2)$  and  $u_{\tilde{l}} \equiv \tilde{l}/l_0$ , that is exactly the same as the variable  $z$  in IPA with the substitution  $l \rightarrow \tilde{l}$ . All these transformations allow one to express the total probability in a form similar to the probability in IPA for large values of  $\xi^2$  and a large number of partial harmonics  $n$ , replacing the sum over  $n$  by an integral over  $n$  [17]:

$$W = \frac{1}{2} \alpha M_e \zeta^{1/2} \int_{\tilde{l}_0}^{\infty} d\tilde{l} \int_1^{u_{\tilde{l}}} \frac{du}{u^{3/2} \sqrt{u-1}} \left\{ J_{\tilde{l}}^2(z) + \right. \\ \left. + \xi^2 (2u - 1) \left[ \left( \frac{\tilde{l}^2}{z^2} - 1 \right) J_{\tilde{l}}^2(z) + J_{\tilde{l}}'^2(z) \right] \right\}. \quad (47)$$

Utilizing Watson's representation [51] for the Bessel functions at  $\tilde{l}$ ,  $z \gg 1$  and  $\tilde{l} > z$ ,  $J_{\tilde{l}}(z) = (2\pi\tilde{l} \tanh \alpha)^{-1/2} \exp[-\tilde{l}(\alpha - \tanh \alpha)]$  with  $\cosh \alpha = \tilde{l}/z$ , and employing a saddle point approximation in the integration in (47) we find the

total probability of  $e^+e^-$  production as (for details see Appendix)

$$W = \frac{3}{8} \sqrt{\frac{3}{2}} \frac{\alpha M_e \xi}{\zeta^{1/2}} d \exp \left[ -\frac{4\zeta}{3\xi} \left( 1 - \frac{1}{15\xi^2} \right) \right], \quad d = 1 + \frac{\xi}{6\zeta} \left( 1 + \frac{\xi}{8\zeta} \right). \quad (48)$$

This expression resembles the production probability in IPA which is the consequence of the fact that, at  $\xi^2 \gg 1$  in a short pulse, only the central part of the envelope at  $\phi \simeq 0$  is important. In the case of  $\xi/\zeta \ll 1$ , approximating  $d = 1 + \mathcal{O}(\xi/\zeta)$ , the leading order term recovers the Ritus result [17].

For completeness, in Fig. 13, *a*, we present FPA results of a full numerical calculation for finite values of  $\xi^2 \leq 10$  for the hyperbolic secant envelope shape with  $N = 2$  (curves are marked by “stars”) and the asymptotic probability cal-

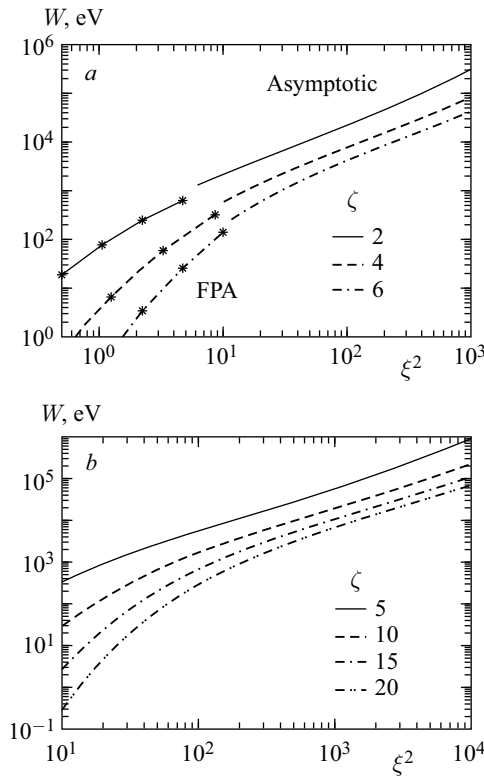


Fig. 13. The total probability  $W$  of the  $e^+e^-$  pair production as a function of  $\xi^2$  for various values of  $\zeta$ . *a*) Results of full numerical calculation in FPA for finite values of  $\xi^2 \leq 10$  (curves marked by “stars” in “FPA” sections) and the asymptotic probability (48) for large values of  $\xi^2$  (sections labeled by “asymptotic”) at  $\zeta = 2, 4,$  and  $6$ . *b*) The asymptotic probability (48) for various values of  $\zeta$  as indicated in the legend

culated by Eq. (48) at  $\zeta = 2, 4$ , and  $6$ , shown by solid, dashed, and dash-dotted curves, respectively. The transition region between the two regimes is in the neighborhood of  $\xi^2 \simeq 10$ . In Fig. 13, *b*, we show the production probability at asymptotically large values of  $\xi^2$  for  $5 \leq \zeta \leq 20$ . The exponential factor in (48) is most important at relatively low values of  $\xi^2 \sim 10$  (large  $\zeta/\xi$ ). At extremely large values of  $\xi^2$  (small  $\zeta/\xi$ ), the pre-exponential factor is dominant.

**2.6. Ultrashort Pulses.** In this section, we consider  $e^+e^-$  pair production due to interaction of the probe photon with an ultrashort pulse, where the number of cycles is less than one.

*2.6.1.  $e^+e^-$  Pair Production at Small Field Intensity ( $\xi^2 \ll 1$ ).* Consider first the case of small field intensity and a finite subthreshold parameter  $\zeta$  characterized by the relations  $z \ll 1$  or  $\xi\zeta \ll 1$ .

The basic functions  $Y_l$  in Eq. (30) can be expressed in this regime as

$$Y_l = \frac{1}{2\pi} \int_{-\infty}^{\infty} d\phi e^{il\phi} f(\phi) g(\phi), \quad (49)$$

with

$$g(\phi) \simeq e^{-ic} e^{-il\xi \cos \phi_0 \phi}, \quad (50)$$

where  $c = z \int_{-\infty}^0 d\phi' f(\phi') \cos(\phi' - \phi_0) - l\phi_0$  is independent of  $\phi$ . As a result, one gets

$$|Y_l| \simeq |F(l(1 - \xi \cos \phi_0))| \simeq |F(l)|, \quad (51)$$

where  $F(l)$  is the Fourier transform of the envelope function  $f(\phi)$ . Keeping the leading terms in Eq. (30) with  $Y_{l-1}^2 \simeq F^2(l-1)$ , one can obtain an approximate expression for the total production probability:

$$W = \alpha M_e \zeta^{1/2} \xi^2 \int_{\zeta}^{\infty} dl \Phi(l) F^2(l-1), \quad (52)$$

with

$$\Phi(l) = v \int_0^1 d \cos \theta \left( \frac{u}{u_l} - \frac{u^2}{u_l^2} + u - \frac{1}{2} \right), \quad (53)$$

where  $u = 1/(1 - v^2 \cos^2 \theta)$ ;  $\theta$  and  $v$  are the polar angle and the velocity of the outgoing electron (positron) in the  $e^+e^-$  c.m.s., respectively:  $v = \sqrt{1 - \zeta/l}$ . An explicit calculation results in

$$\Phi(l) = \frac{1}{2} \left\{ \left( 1 + \frac{\zeta}{l} - \frac{\zeta^2}{2l^2} \right) \log \frac{1+v}{1-v} - v \left( 1 + \frac{\zeta}{l} \right) \right\}. \quad (54)$$

The Fourier transforms of the hs and sF envelope functions are given in Eq. (38), and for illustration, the square of the Fourier transforms for a subcycle pulse with  $N = 0.5$  are exhibited in Fig. 14. Figure 14, *a* corresponds to the hyperbolic secant shape. One can see a fast monotonic decrease of  $F_{\text{hs}}$  at large values of  $l$ . The square of the Fourier transform for the symmetrized Fermi shape is shown in Fig. 14, *b*, where the solid, dashed and dot-dashed curves correspond to the ratio  $b/\Delta = 0.15, 0.3,$  and  $0.5,$  respectively. One can see large qualitative and quantitative differences between the one-parameter and flat-top symmetrized Fermi shapes, in particular, at  $b/\Delta \leq 0.3$ . In the second case,  $F^2$  decreases exponentially as  $\exp[-2\pi\Delta(b/\Delta)]$ . The slope decreases proportionally to  $b/\Delta$  (at fixed  $\Delta$ ). Also, the function oscillates with the half-cycle  $\delta l = \pi/\Delta = \pi/0.5\pi = 2$ . Contrary to the above one-parameter shapes, the function  $F_{\text{sF}}$  has a significant high- $l$  component at  $2 \leq l \leq 4$ . This strong effect is not seen in the  $\phi$  space (cf. Fig. 4, right top and middle top panels), where all envelope functions

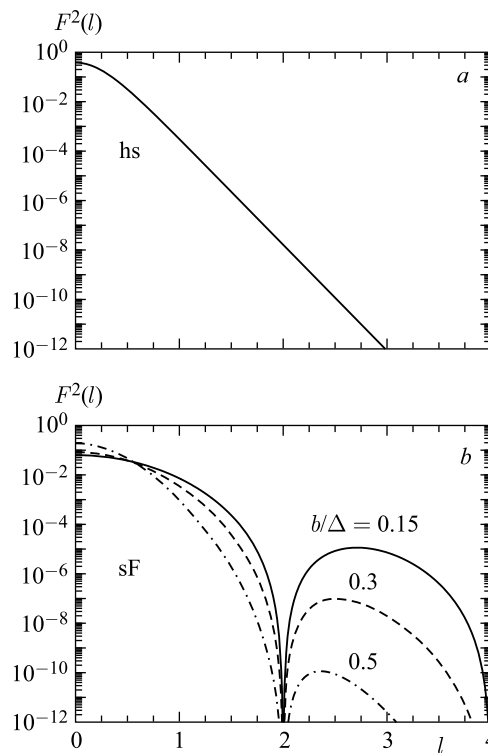


Fig. 14. Square of the Fourier transforms of the envelope functions for a subcycle pulse with  $N = 0.5$ . *a*) The hyperbolic secant shape. *b*) The solid, dashed and dash-dotted curves show the symmetrized Fermi shape for  $b/\Delta = 0.15, 0.3,$  and  $0.5,$  respectively

look similar to each other. However, the difference in  $l$ -space is very important for the pair production.

Our prediction for the total probability of  $e^+e^-$  pair production as a function of the subthreshold parameter  $\zeta$  for the one-parameter envelope functions for an ultrashort pulse with  $N = 0.5$  is shown in Fig. 15. The solid curves exhibit result of full numerical calculations using Eq.(26) with the hyperbolic secant shape. The symbols “star” display the result obtained by using the approximation (52). The thin solid curves marked by dots correspond to the IPA case. Figure 15, *a* and *b* display results for  $\xi^2 = 10^{-2}$  and  $10^{-4}$ , respectively. One can see the identity of predictions for the ultrashort pulse and IPA near and above the threshold at  $\zeta \lesssim 1$ , and a strong difference between them below the threshold, i.e., for  $\zeta > 1$ . Our approximate (analytical) solution of Eq.(52) is in a fairly good agreement

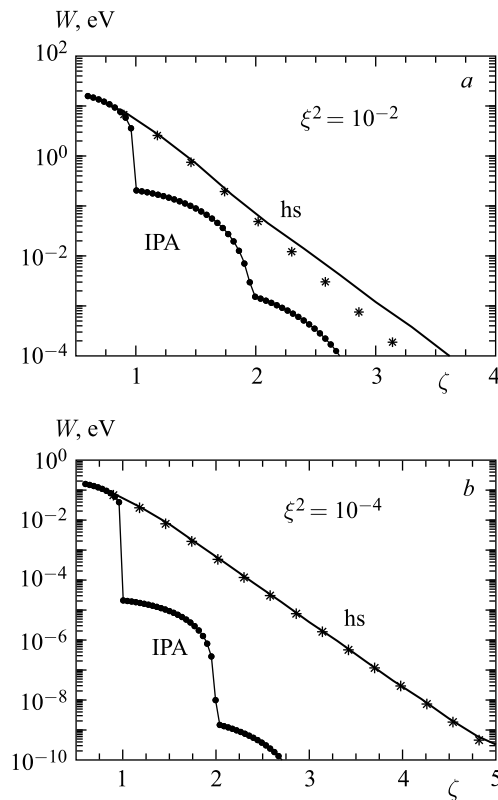


Fig. 15. The probability  $W$  of  $e^+e^-$  production as a function of the subthreshold parameter  $\zeta$  for one-parameter hs envelope functions for an ultrashort pulse with  $N = 0.5$ . The symbols “star” are for the approximation (52). The thin solid curves marked by dots correspond to IPA. Panels *a* and *b* are for  $\xi^2 = 10^{-2}$  and  $10^{-4}$ , respectively

with the full numerical calculation. The function  $\Phi(l)$  in Eq. (52) is rather smooth compared to the Fourier transform  $F(l-1)$ , therefore, the dominant contribution to the integral in Eq. (52) comes from the lower limit of  $l$ , and qualitatively, the slope of the probability as a function of  $\zeta$  is determined by the scale parameter  $\Delta$  of the envelope functions

$$W_{\text{hs}}(\zeta) \sim \exp[-\pi\Delta\zeta]. \tag{55}$$

Despite of the exponential decrease of the probability  $W$  as a function of  $\zeta$ , one can see a large difference (several orders of magnitude) between predictions for the ultrashort pulse and IPA. In the latter case the probability decreases much faster with increasing  $\zeta$ .

Our results for the symmetrized Fermi envelope are presented in Fig. 16. Now, the shape of the probability is determined by the two parameters  $b$

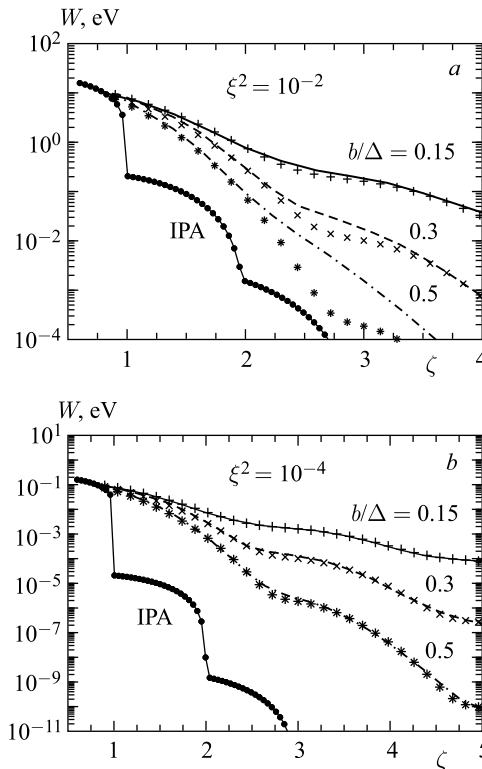


Fig. 16. The same as in Fig. 15, but for symmetrized Fermi shape envelope. The solid, dashed, and dash-dotted curves are for  $b/\Delta = 0.15, 0.3,$  and  $0.5,$  respectively. The corresponding approximate solutions are shown by pluses, crosses, and stars, respectively



(or  $b/\Delta$ ) and  $\Delta$

$$W_{\text{sF}}(\zeta) \sim \exp \left[ -2\pi\Delta \frac{b}{\Delta} \zeta \right] \sin^2 \Delta\zeta. \quad (56)$$

The first term describes the slope of the probability as a function of  $\zeta$ . The slope is proportional to the “ramping time” of the envelope function  $b$  (or to the ratio  $b/\Delta$  at fixed  $\Delta$ ). The second term, following from the Fourier transform shown in Fig. 14, describes some oscillations with a period inversely proportional to the duration  $\Delta$  of the flat-top envelope and is independent of the ramping parameter  $b$ . Again, one can see a great difference between results for the ultrashort pulse and IPA on qualitative and quantitative levels. The probability in IPA has a typical step-like behavior, where each new step indicates the contribution of the next integer harmonic. In FPA, the probability decreases monotonically with a slope determined by the shape of the envelope. The quantitative difference is rather large and, as indicated by results shown in Figs. 15 and 16, can reach orders of magnitude depending on the shape of the envelope.

*2.6.2. Intermediate Field Intensity, Anisotropy.* As we have shown above, at small values of  $z$ ,  $z \ll 1$ , the probability of  $e^+e^-$  production is essentially determined by the pulse shape. The function  $g(\phi)$  in Eq. (49) is not important and, therefore, the total probability would be isotropic with respect to the azimuthal angle  $\phi_e = \phi_0$  because only the function  $\mathcal{P}(\phi)$  in Eq. (20) contains a  $\phi_0$  dependence. For finite values of  $z$ , however, the function  $g(\phi)$  becomes important, and the electron (positron) azimuthal angle distribution is anisotropic relative to the direction of the vector  $\mathbf{a}_x \equiv \mathbf{a}_1$  in Eq. (1), at least for the monotonically rapidly decreasing one-parameter envelope shapes. The reason of such anisotropy is the following. At finite values of  $z$ , the function  $Y(l)$  in Eq. (49) is determined by the integral over  $d\phi$  with a rapidly oscillating function proportional to the exponent in

$$\exp \left\{ i \left[ l\phi - z \left( \cos \phi_0 \int_{-\infty}^{\phi} d\phi' f(\phi') \cos \phi' + \sin \phi_0 \int_{-\infty}^{\phi} d\phi' f(\phi') \sin \phi' \right) \right] \right\}. \quad (57)$$

In the case of a fast-decreasing function  $f(\phi')$ , the contribution of the term proportional to  $\sin \phi_0$  is much smaller compared to the term proportional to  $\cos \phi_0$ , because the functions  $f(\phi')$  and  $\sin \phi'$  in the second integral are in “antiphase”. At finite  $z$ , the dominant contribution to the functions  $Y_l$  comes from the region where the difference in the exponent is minimal, i.e.,  $\phi_e = \phi_0 \simeq 0$ . This means that the electrons would be emitted mostly along the vector  $\mathbf{a}_x$  and the positrons in the opposite direction.

We define the anisotropy of the electron emission as

$$\mathcal{A} = \frac{dW(\phi_e) - dW(\phi_e + \pi)}{dW(\phi_e) + dW(\phi_e + \pi)}. \quad (58)$$

The differential probability of the  $e^+e^-$  pair emission and the anisotropy as functions of the azimuthal angle  $\phi_e$  are exhibited in Fig. 17. The calculations are for the fast-decreasing one-parameter hs envelope functions for  $\Delta = 0.5\pi$ ,  $\zeta = 4$  and  $\xi^2 = 0.1$ . One can see a rapidly decreasing probability with  $\phi_e$  which leads to the strong anisotropy of electron (positron) emission.

In the case of the symmetrized Fermi distribution with small  $b/\Delta$ , the situation changes drastically. As  $b/\Delta \rightarrow 0$ , the envelope function goes to the flat-top (step-like) shape  $f_{Fs}(\phi) \rightarrow \theta(\Delta^2 - \phi^2)$  with  $\theta(x) = 1, 0$  for  $x \geq 0$  or  $x < 0$ , respectively, and correspondingly

$$Y_l \simeq \frac{1}{2\pi} \int_{-\Delta}^{\Delta} d\phi e^{i[\tilde{l}\phi - z \sin(\phi - \phi_0)]}, \tag{59}$$

with  $\tilde{l} = l + \xi^2\zeta u$ . The function  $Y_l$  in the region  $\zeta \leq l < l_{\max} \gg 1$  is alternating, rapidly oscillating with an amplitude that depends only on  $\xi$ ,  $\zeta$ , and  $u$ . It is not sensitive to  $\phi_0$ . A change in  $\phi_0$  leads to some phase shift of  $Y(l)$  in a range of integration, leaving  $\langle |Y_l|^2 \rangle$  to be independent of  $\phi_0$ . Therefore, the dependence of the integral of the partial probability  $w(l) \sim |Y_l|^2$  in Eq. (26) on  $\phi_0$  is negligible.

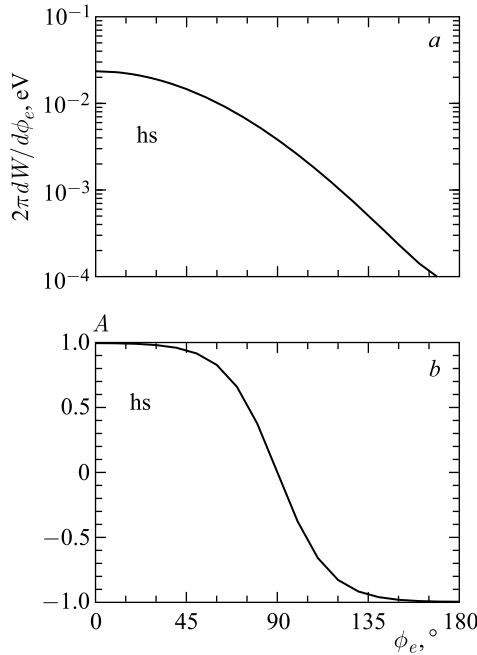


Fig. 17. *a)* The differential production probability as a function of the azimuthal angle  $\phi_e$  of the electron emission. *b)* The anisotropy (58) for the hyperbolic secant shapes. For  $\xi^2 = 0.1$  and  $\zeta = 4$

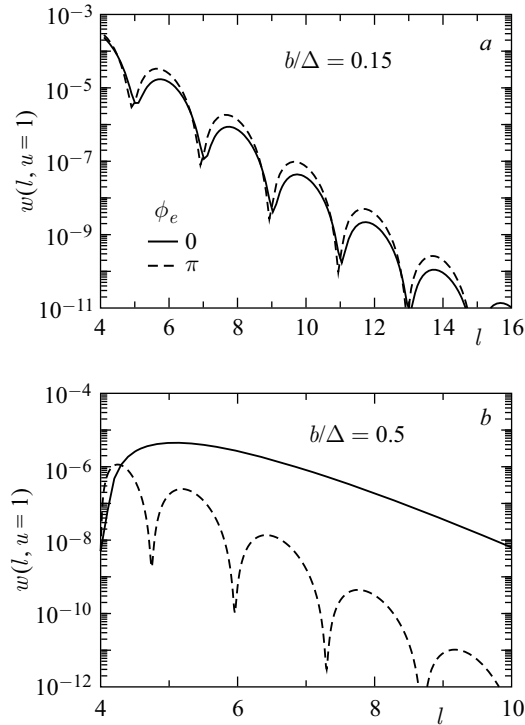


Fig. 18. The partial probability  $w(l)$  defined in (30) at  $\phi_0 = 0$  and  $\pi$  shown by solid and dashed curves, respectively, for the symmetrized Fermi envelope shape. Panel *a* corresponds to small values of  $b/\Delta = 0.15$ , while panel *b* is for  $b/\Delta = 0.5$ . For  $\xi^2 = 0.1$  and  $\zeta = 4$

As an example, in Fig. 18, *a*, we present the partial probability  $w(l)$  as a function of  $l$ , calculated at  $\xi^2 = 0.1$ ,  $\zeta = 4$ , and  $u = 1$  for the small values of  $b/\Delta$  equal to 0.15 at  $\phi_0 = 0$  and  $\pi$ , shown by solid and dashed curves, respectively. One can see some small modification of the frequency of oscillations at  $l \sim l_{\min} = \zeta$  at two extreme values of  $\phi_0$ , but the amplitudes of the oscillations are close to each other. This situation is quite different from the case of a large value of  $b/\Delta = 0.5$  exhibited in Fig. 18, *b*. One can see a strong difference in the  $l$  dependence of  $w(l)$  for  $\phi_0 = 0$  and  $\pi$ . In the first case, the function  $w(l)$  has only one oscillation in a wide range of  $l$  and decreases smoothly with  $l$ . In the second case, the probability has a number of oscillations decreasing rapidly with increasing  $l$ . As a result, the total probability in the second case is much smaller.

In Fig. 19, we present our results for the symmetrized Fermi shape for the production probability (plot *a*) and for the anisotropy (plot *b*) for  $b/\Delta = 0.15$

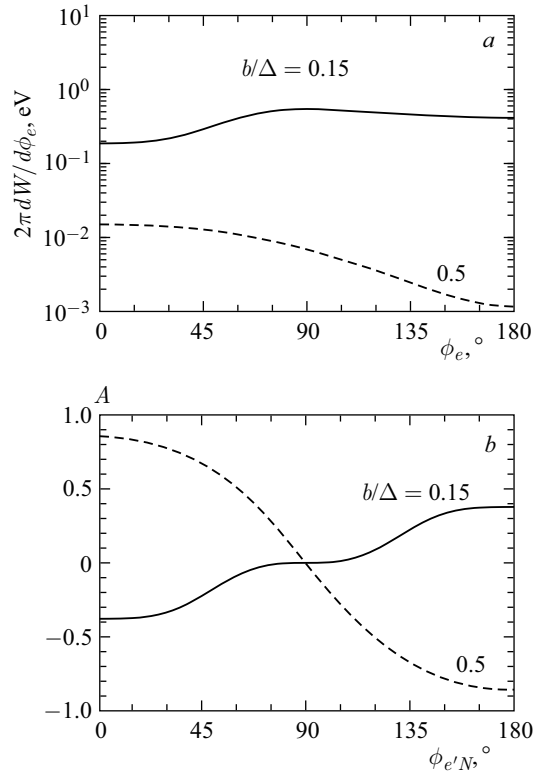


Fig. 19. The same as in Fig. 17, but for the symmetrized Fermi shape. The solid and dashed curves are for  $b/\Delta = 0.15$  and 0.5, respectively

and 0.5. The result for  $b/\Delta = 0.5$  is similar to that shown in Fig. 17. However, for smaller values of  $b/\Delta$ , the probability is a smooth function of  $\phi_e$  which leads to a small absolute value of the anisotropy.

**2.7. Effect of the Finite Carrier Phase.** Consider now the impact of the finite carrier phase  $\tilde{\phi}$  in the e.m. potential (1) for the  $e^+e^-$  production. In the case of finite  $\tilde{\phi}$ , the functions  $C_l^{(i)}$  in the transition matrix (18) are modified as follows:

$$C^{(0)}(l) = \frac{1}{2\pi l} \int_{-\infty}^{\infty} d\phi (z \cos(\phi - \phi_0 + \tilde{\phi}) f(\phi) - \xi^2 \zeta u f^2(\phi)) e^{il\phi - i\mathcal{P}(\phi)},$$

$$C^{(1)}(l) = \frac{1}{2\pi} \int_{-\infty}^{\infty} d\phi f^2(\phi) e^{il\phi - i\mathcal{P}(\phi)},$$

$$\begin{aligned}
C^{(2)}(l) &= \frac{1}{2\pi} \int_{-\infty}^{\infty} d\phi f(\phi) \cos(\phi + \tilde{\phi}) e^{il\phi - i\mathcal{P}(\phi)}, \\
C^{(3)}(l) &= \frac{1}{2\pi} \int_{-\infty}^{\infty} d\phi f(\phi) \sin(\phi + \tilde{\phi}) e^{il\phi - i\mathcal{P}(\phi)},
\end{aligned} \tag{60}$$

with

$$\mathcal{P}(\phi) = z \int_{-\infty}^{\phi} d\phi' \cos(\phi' - \phi_0 + \tilde{\phi}) f(\phi') - \xi^2 \zeta u \int_{-\infty}^{\phi} d\phi' f^2(\phi'). \tag{61}$$

Utilizing the new basic functions

$$\begin{aligned}
Y_l(z) &= \frac{1}{2\pi} e^{-il(\phi_0 - \tilde{\phi})} \int_{-\infty}^{\infty} d\phi f(\phi) e^{il\phi - i\mathcal{P}(\phi)}, \\
X_l(z) &= \frac{1}{2\pi} e^{-il(\phi_0 - \tilde{\phi})} \int_{-\infty}^{\infty} d\phi f^2(\phi) e^{il\phi - i\mathcal{P}(\phi)},
\end{aligned} \tag{62}$$

one can obtain the following representation of the functions  $C^{(i)}(l)$ :

$$\begin{aligned}
C^{(0)}(l) &= \tilde{Y}_l(z) e^{il(\phi_0 - \tilde{\phi})}, \\
\tilde{Y}_l(z) &= \frac{z}{2l} (Y_{l+1}(z) + Y_{l-1}(z)) - \xi^2 \frac{u}{u_l} X_l(z), \\
C^{(1)}(l) &= X_l(z) e^{il(\phi_0 - \tilde{\phi})}, \\
C^{(2)}(l) &= \frac{1}{2} \left( Y_{l+1} e^{i(l+1)\phi_0} + Y_{l-1} e^{i(l-1)\phi_0} \right) e^{-il\tilde{\phi}}, \\
C^{(3)}(l) &= \frac{1}{2i} \left( Y_{l+1} e^{i(l+1)\phi_0} - Y_{l-1} e^{i(l-1)\phi_0} \right) e^{-il\tilde{\phi}},
\end{aligned} \tag{63}$$

which allows one to express the partial probabilities  $w(l)$  in Eq. (27) in the form of Eq. (30) but with the new basic functions (62). We recall that  $\phi_0$  in the above expressions is equal to the azimuthal angle  $\phi_e$  of the outgoing electron momentum in c.m.s.

It is natural to expect that the effect of the finite carrier phase essentially appears in the azimuthal angle distribution of the outgoing electron, because the carrier phase is included in the expressions for the basic functions (62) in the combination  $\phi_e - \tilde{\phi}$ .

As an example, in Fig. 20, *a* we show the probability of  $e^+e^-$  production as a function of the azimuthal angle  $\phi_e$  for different values of the carrier phase  $\tilde{\phi}$

for the subcycle pulse with  $N = 0.5$  for a hyperbolic secant shape with  $\zeta = 4$  and  $\xi^2 = 0.1$ . One can see a clear bump-like structure of the distribution, where the bump position coincides with the corresponding value of the carrier phase. The reason of such a behaviour is the same as an alignment of the probability along  $\phi_e = 0$  for  $\tilde{\phi} = 0$  described in the previous subsection. Indeed, now the basic functions  $Y_l$  and  $X_l$  are determined by the integral over  $d\phi$  with a rapidly oscillating function proportional to the exponent

$$\exp \left\{ i \left[ l\phi - z \left( \cos(\phi_e - \tilde{\phi}) \int_{-\infty}^{\phi} d\phi' f(\phi') \cos \phi' + \sin(\phi_e - \tilde{\phi}) \int_{-\infty}^{\phi} d\phi' f(\phi') \sin \phi' \right) \right] \right\}. \quad (64)$$

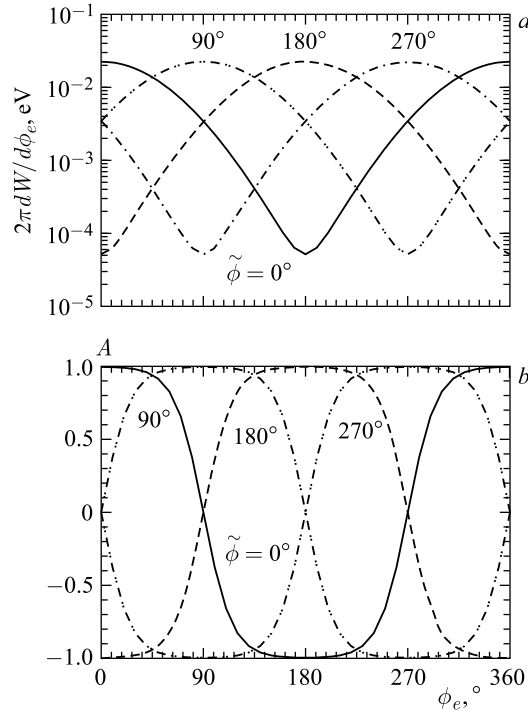


Fig. 20. *a*) The production probability as a function of the azimuthal angle of the direction of flight of the outgoing electron  $\phi_e$  for different values of the carrier phase  $\tilde{\phi}$ . The solid, dot-dot-dashed, dashed and dash-dotted curves are for the carrier phase equal to 0, 90, 180 and 270 degrees, respectively. *b*) The anisotropy (58) for different values of  $\tilde{\phi}$ . For the hyperbolic secant shape with  $N = 0.5$ ;  $\xi^2 = 0.1$  and  $\zeta = 4$

Then, taking into account the inequality

$$\int_{-\infty}^{\phi} d\phi' f(\phi') \cos \phi' \gg \int_{-\infty}^{\phi} d\phi' f(\phi') \sin \phi', \quad (65)$$

which is valid for the subcycle pulse with hyperbolic secant shape, one can conclude that the main contribution to the probability comes from the region  $\phi_e \simeq \tilde{\phi}$ , which is confirmed by the result of our full calculation shown in Fig. 20, *a*.

The corresponding anisotropies defined by Eq. (58) are exhibited in Fig. 20, *b*. One can see a strong dependence of the anisotropy on the carrier phase which leads to the “bump” structure of the differential probabilities shown in the left panel. The anisotropy takes a maximum value  $\mathcal{A} \simeq 1$  at  $\phi_e = \tilde{\phi}$  and  $|\mathcal{A}| < 1$  at  $\phi_e \neq \tilde{\phi}$ . It takes a minimum value  $\mathcal{A} \simeq -1$  at  $\phi_e - \tilde{\phi} = \pm\pi$ .

The effect of the carrier phase decreases when the duration of pulse increases. Thus, when the number of oscillations in a pulse is  $N \geq 2$ , the inequality of two terms in (65) does not hold, instead they have the same order of magnitude and the alignment of the differential distributions with respect to  $\phi_e \simeq \tilde{\phi}$  becomes

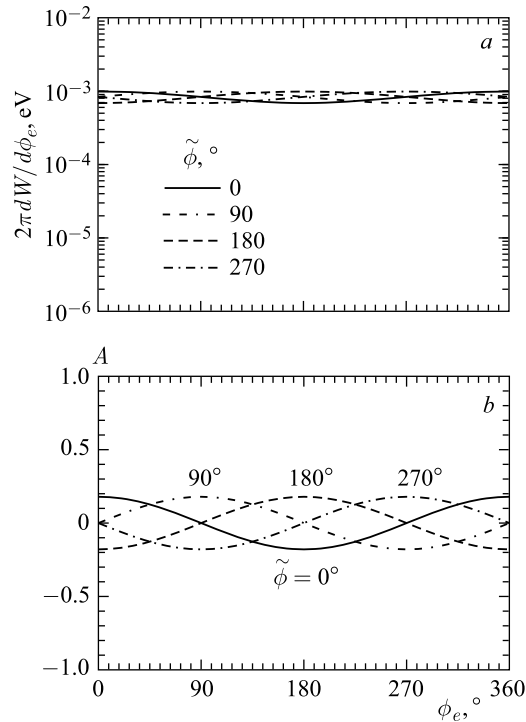


Fig. 21. The same as in Fig. 20, but for short pulse with  $N = 2$

very weak. The corresponding results are exhibited in Fig. 21. The probabilities (rates)  $2\pi dW/d\phi_e$  as a function of  $\phi_e$  for the short pulse with  $N = 2$ ,  $\zeta = 4$  and  $\xi^2 = 0.1$  for different  $\tilde{\phi}$  are shown in Fig. 21, *a*. One can see a very weak dependence of the rates on  $\phi_e$  and  $\tilde{\phi}$ . The rates are concentrated near the value  $\sim 10^{-3}$  eV. Although, a small enhancement in the vicinity of  $\phi_e \simeq \tilde{\phi}$  still exists. This also is manifest in the anisotropy shown in Fig. 21, *b*. The anisotropy is finite, but its absolute value is less than 0.2.

In order to stress the alignment of the differential azimuthal-angle distributions along  $\phi_e \simeq \tilde{\phi}$ , one can plot differential distributions and anisotropies as a function of the “scale” variable  $\Phi = \phi_e - \tilde{\phi}$ . In this case, all curves shown, for example, in Fig. 20, *a*, are merged into a single carrier phase independent curve. The corresponding result is exhibited in Fig. 22, where one can see a carrier phase independence of the differential distributions and anisotropies shown in panels *a* and *b*, respectively. Similarly, a carrier phase independent result is obtained for the short pulse with  $N = 2$  shown in Fig. 23.

Formally, this follows from the fact that the carrier phase is included in the expressions for the basic functions (62) and (63) in the combination  $\phi_e - \tilde{\phi}$ .

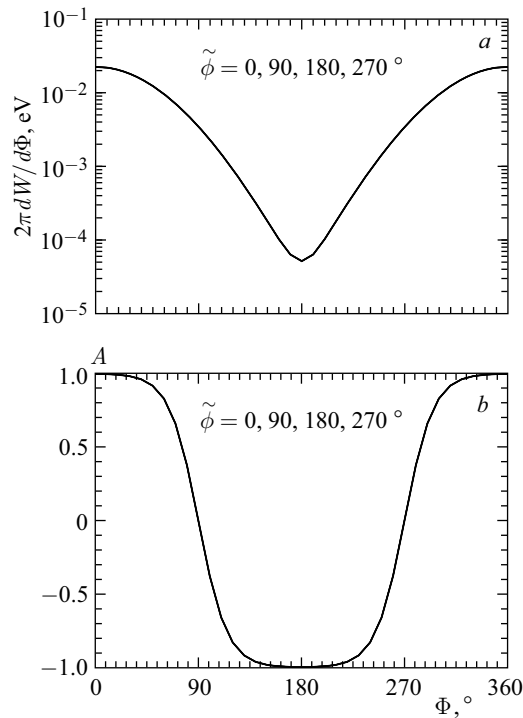


Fig. 22. The same as in Fig. 20, but as a function of the scale variable  $\Phi = \phi_e - \tilde{\phi}$



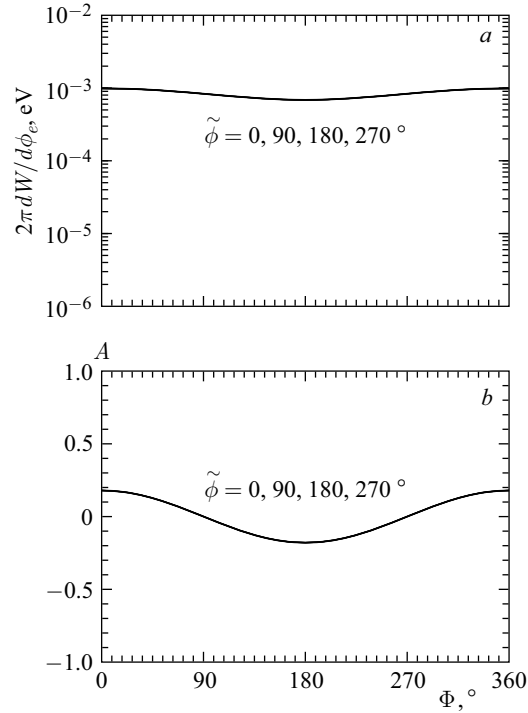


Fig. 23. The same as in Fig. 21, but as a function of the scale variable  $\Phi = \phi_e - \tilde{\phi}$

Therefore, the differential distributions are a function of  $\Phi = \phi_e - \tilde{\phi}$  rather than of  $\phi_e$  (for finite  $\tilde{\phi}$ ). From the physical point of view, this means that at finite  $\tilde{\phi}$  the differential azimuthal distributions are convenient to study in the coordinates  $x', y'$  rotated relative to the initial coordinates  $x, y$  by an angle equal to the carrier phase  $\tilde{\phi}$ .

### 3. COMPTON SCATTERING IN SHORT LASER PULSE

**3.1. General Formalism.** The Compton scattering process is considered here as a spontaneous emission of one photon off an electron in an external e.m. field. Similarly to the Breit–Wheeler process, we employ the four-potential of a circularly polarized laser field in the form of Eq. (1) with the envelope function  $f(\phi)$  discussed in Sec. 1. Here, we also use one-parameter hyperbolic secant (hs) envelope and two-parameter symmetrized Fermi (sF) shape with  $b/\Delta = 0.15$ . All details and notations are given in Sec. 1. Using the same arguments as before, we start our consideration assuming  $\tilde{\phi} = 0$  and discuss the impact of the finite carrier phase later.

Utilizing the e.m. potential (1) and the Volkov solution for the electron wave function in this background field, one finds the following expression for the  $S$ -matrix element:

$$S = -ie \int_{-\infty}^{\infty} dl M(l) \frac{(2\pi)^4 \delta^4(p + lk - p' - k')}{\sqrt{2E 2E' 2\omega'}}, \quad (66)$$

where  $k, k' = (\omega', \mathbf{k}')$ ,  $p = (E, \mathbf{p})$ , and  $p' = (E', \mathbf{p}')$  refer to the four-momenta of the background (laser) field (1), scattered photon, as well as asymptotic incoming (in-state) and outgoing (out-state) electrons. All quantities are considered in the laboratory system. Similarly to the Breit–Wheeler process the transition matrix  $M(l)$  consists of four terms (cf. Eq. (18)),

$$M(l) = \sum_{i=0}^3 M^{(i)} C^{(i)}(l), \quad (67)$$

where the transition operators have now the form  $M^{(i)} = \bar{u}_{p'} \hat{M}^{(i)} u_p$ , with

$$\begin{aligned} \hat{M}^{(0)} &= \not{\epsilon}', \\ \hat{M}^{(1)} &= \frac{e^2 a^2 (\epsilon' \cdot k) \not{k}}{2(k \cdot p)(k \cdot p')}, \\ \hat{M}^{(2,3)} &= \frac{e \not{\epsilon}'_{(1,2)} \not{k} \not{\epsilon}'}{2(k \cdot p')} + \frac{e \not{\epsilon}' \not{k} \not{\epsilon}'_{(1,2)}}{2(k \cdot p)}. \end{aligned} \quad (68)$$

Here,  $u_p$  and  $\bar{u}_{p'}$  are free Dirac spinors depending on the momenta  $p$  and  $p'$ ; and  $\epsilon'$  denotes the polarization four-vector of the scattered photon. Since the Compton scattering is the crossing channel of the Breit–Wheeler processes, the identity  $\hat{M}_{\text{Compt}}^{(i)}(p, p', k, k') = \hat{M}_{\text{BW}}^{(i)}(-p, p', k, -k')$  is realized. Utilizing the prescription of Subsec. 2.1 one can express the coefficients  $C^{(i)}(l)$  through basic functions  $Y_l(z)$  and  $X_l(z)$  (cf. Eqs. (28) and (29)) with

$$\mathcal{P}(\phi) = z \int_{-\infty}^{\phi} d\phi' \cos(\phi' - \phi_0) f(\phi') - \xi^2 \frac{u}{u_0} \int_{-\infty}^{\phi} d\phi' f^2(\phi') \quad (69)$$

and

$$z = 2l\xi \sqrt{\frac{u}{u_l} \left(1 - \frac{u}{u_l}\right)}, \quad u \equiv \frac{(k' \cdot k)}{(k \cdot p')}, \quad u_l = \frac{l}{u_0}, \quad (70)$$

where  $u_0 = 2k \cdot p/m^2$ . Now, the phase  $\phi_0$  is equal to the azimuthal angle of the direction of flight of the outgoing electron,  $\phi_0 = \phi_{e'}$ , and it is related to the azimuthal angle of the momentum of the outgoing photon as  $\phi_{\gamma'} = \phi_0 + \pi$ .

This representation of functions  $C^{(i)}(l)$  allows one to define a partial differential cross section

$$\frac{d\sigma(l)}{d\omega' d\phi_{e'}} = \frac{2\alpha^2}{N_0 \xi^2 (s - m^2) |p - l\omega|} w(l), \quad (71)$$

with

$$w(l) = -2\tilde{Y}_l^2(z) + \xi^2 \left( 1 + \frac{u^2}{2(1+u)} \right) \times \\ \times \left( Y_{l-1}^2(z) + Y_{l+1}^2(z) - 2\tilde{Y}_l(z)X_l^*(z) \right). \quad (72)$$

Equation (72) resembles the corresponding expression for the partial probability of photon emission in the case of IPA [50] with the substitutions  $l \rightarrow n = 1, 2, \dots$  and  $\tilde{Y}_l^2(z)$ ,  $Y_l^2(z)$ ,  $\tilde{Y}_l(z)X_l^*(z) \rightarrow J_n^2(z')$ , namely:

$$w_n = -2J_n^2(z') + \xi^2 \left( 1 + \frac{u^2}{2(1+u)} \right) \times \\ \times \left( J_{n-1}^2(z') + J_{n+1}^2(z') - 2J_n^2(z') \right), \quad (73)$$

where  $J_n(z')$  denotes Bessel functions with  $z' = \frac{2n\xi}{\sqrt{1+\xi^2}} \sqrt{\frac{u}{u_n} \left( 1 - \frac{u}{u_n} \right)}$  and  $u_n = \frac{2n(k \cdot p)}{m^2(1+\xi^2)}$ . Similarly to IPA, the phase  $\phi_0$  can be determined through invariants  $\alpha_{1,2}$  as  $\cos \phi_0 = \alpha_1/z$ ,  $\sin \phi_0 = \alpha_2/z$  with  $\alpha_{1,2} = e(a_{1,2} \cdot p/k \cdot p - a_{1,2} \cdot p'/k \cdot p')$ . The dimensionless field intensity  $\xi^2$  is described by Eqs. (2)–(6).

The frequency  $\omega'$  of the emitted photon is related to the auxiliary variable  $l$  and the polar angle  $\theta'$  of the direction of the momentum  $\mathbf{k}'$  via

$$\omega' = \frac{l\omega(E + |\mathbf{p}|)}{E + |\mathbf{p}| \cos \theta' + l\omega(1 - \cos \theta')} \quad (74)$$

and increases with  $l$  at fixed  $\theta'$  since  $\omega'$  is a function of  $l$  at fixed  $\theta'$ . For convenience, we also present a similar expression for IPA, where the fermions are dressed and the integer quantity  $n$ , together with the field intensity  $\xi^2$ , appear:

$$\omega' = \frac{n\omega(E + |\mathbf{p}|)}{E + |\mathbf{p}| \cos \theta' + \omega \left( n + \frac{m^2 \xi^2}{2(k \cdot p)} \right) (1 - \cos \theta')}. \quad (75)$$

The differential cross section of the one-photon production is eventually

$$\frac{d\sigma}{d\omega'} = \int_{\eta} dl \int_0^{2\pi} d\phi_{e'} \frac{d\sigma(l)}{d\omega' d\phi_{e'}} \delta(l - l(\omega')). \quad (76)$$

The lower integration limit  $\eta > 0$  is defined by kinematics, i.e., by the minimum value of the considered  $\omega'$ , in accordance with Eq. (74). In the IPA case, the variable  $n = 1, 2, \dots$  refers to the contribution of the individual harmonics ( $n = 1$  with  $\xi^2 \ll 1$  recovers the Klein–Nishina cross section, cf. [17]). The value  $n\omega$  is related to the energy of the background field involved in Compton scattering. Obviously, this value is a multiple of  $\omega$ . In FPA, the internal quantity  $l$  is a continuous variable, implying a continuous distribution of the differential cross section over the  $\omega' - \theta'$  plane. The quantity  $l\omega$  can be considered as energy of the laser beam involved in the Compton process, which is not a multiple  $\omega$ . Mindful of this fact, without loss of generality, we denote the processes with  $l > 1$  as a multiphoton generalized Compton scattering, remembering that  $l$  is a continuous quantity.

The multiphoton effects become most clearly evident in the partially energy-integrated cross section

$$\bar{\sigma}(\omega') = \int_{\omega'}^{\infty} d\bar{\omega}' \frac{d\sigma(\bar{\omega}')}{d\bar{\omega}'} = \int_{l'}^{\infty} dl \frac{d\sigma(l)}{dl}, \quad (77)$$

where  $\frac{d\sigma(l)}{dl} = \left( \frac{d\sigma(\omega')}{d\omega'} \right) \left( \frac{d\omega'(l)}{dl} \right)$ , and the minimum value of  $l'$  is

$$l' = \frac{\omega'}{\omega} \frac{E + |\mathbf{p}| \cos \theta'}{E + |\mathbf{p}| - \omega'(1 - \cos \theta')}. \quad (78)$$

The cross section (77) has the meaning of a cumulative distribution. In this case, the subthreshold multiphoton events correspond to frequencies  $\omega'$  of the outgoing photon which exceed the corresponding threshold value  $\omega'_1 = \omega'(l = 1)$  (cf. Eq. (74)), and ratio  $\kappa = \omega'/\omega'_1 > 1$  represents the subthreshold parameter.

**3.2. The Differential Cross Section.** In IPA [17, 50], the cross section of the multiphoton Compton scattering increases with  $\theta'$  towards  $180^\circ$ . For instance, it peaks at about  $170^\circ$  for the chosen electron energy of 4 MeV (all quantities are considered in the laboratory frame) and rapidly drops to zero when  $\theta'$  approaches  $180^\circ$  for the harmonics  $n > 1$  yielding thus the blind spot for back-scattering. Therefore, in our subsequent analysis we choose the near-backward photon production at  $\theta' = 170^\circ$  and an optical laser with  $\omega = 1.55$  eV. Defining one-photon events by  $n = 1$ , this kinematics leads via Eq. (75) to  $\omega'_1 \equiv \omega'(n = 1, \xi^2 \ll 1, \theta' = 170^\circ) \simeq 0.133$  keV which we refer to as a threshold value. Accordingly,  $\omega' > \omega'_1$  is enabled by nonlinear effects, which, in turn, may be related loosely to multiphoton dynamics with  $n > 1$  in IPA or  $l > 1$  in FPA where, we remind again, the internal variable  $l$  cannot be interpreted strictly as a number of laser photons involved (cf. [52]). Note that all calculations for IPA are performed in a standard way [17, 50]. The energy of the outgoing photon in

IPA is calculated using Eq.(75), where dressing of electrons in the background field is taken into account.

Let us consider first an example of short pulses with moderate intensity,  $\xi^2 = 10^{-3}$ , similar to a recent experiment of the Compton back-scattering [53]. Results for the hs and sF shapes are exhibited in Fig.24. The solid and dashed curves correspond to pulses with  $N = 2$  and 5, respectively. The stars depict the IPA results, i.e., the harmonics at fixed scattering angle  $\theta'$ . Their positions correspond to integer values of  $n = 1, 2, \dots$  in accordance with Eq. (75), i.e., the distribution of scattered photon energies is a discrete function of  $\omega'$ . We stress that the cross section at  $\omega' > \omega'_1$  is essentially “subthreshold”, i.e., outside the kinematically allowed region of the Klein–Nishina process due to multiphoton effects.

In the FPA case, the energy distribution becomes a continuous function of  $\omega'$ . The actual shape is determined by both the pulse duration and the envelope form. Consider first the case of the hs shape (cf. Fig.24, *a*). The cross section displays

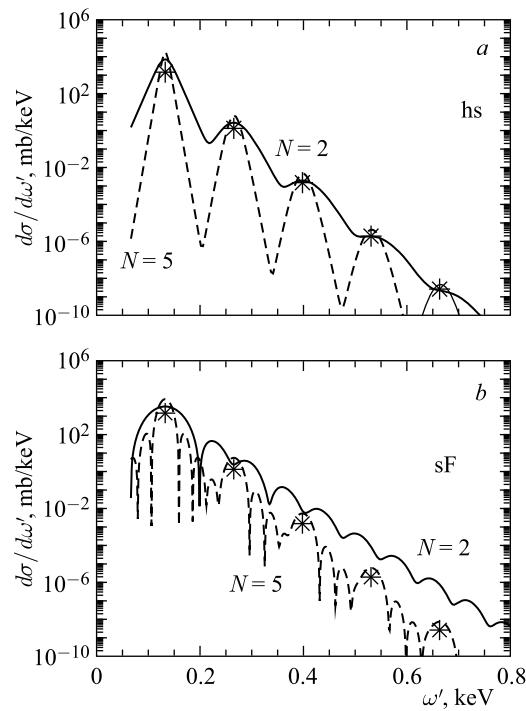


Fig. 24. Differential cross section  $d\sigma/d\omega'|_{\theta'=170^\circ}$  of the Compton scattering for  $\xi^2 = 10^{-3}$ . The solid and dashed curves are for  $N = 2$  and 5, respectively. The stars depict the IPA results for the lowest harmonics. Panels *a* and *b* correspond to hyperbolic secant (hs) and symmetrized Fermi (sF) shapes of the envelopes, respectively

sharp bumps with peak positions corresponding to integer values of  $l = n$  (as in IPA). In the vicinity of the bumps, at  $l = n \pm \epsilon$ ,  $\epsilon \ll 1$ , the cross section is rapidly decreasing. Such a behavior reflects the properties of the functions  $Y_{l=n+\epsilon}(z)$  (cf. Eq.(37)) which is proportional to the Fourier transform of the  $(n + 1)$ -th degree of the envelope function  $F^{(n+1)}(\epsilon)$ . At  $\xi^2 \ll 1$ , the contribution of terms  $\propto X_l$  is negligible.

The behavior of the cross section in the vicinity of the first bump is proportional to  $F_{\text{hs}}^2(\epsilon)$  with  $F_{\text{hs}}(\epsilon)$  given in Eq. (38), or  $F_{\text{hs}}(x) \simeq \Delta \exp[-\pi\Delta x/2]$ . Thus, the cross section becomes steeper with increasing pulse duration  $\Delta$ . This result qualitatively agrees with that of [23].

In the case of the sF shape, the dependence  $F_{\text{sF}}(\epsilon)$  is more complicated (cf. Eq.(38)). Together with the overall decrease of the cross section proportional to  $\exp[-2\pi b l(\omega')]$  it also indicates fast oscillations with a frequency  $\propto \Delta$ . Such

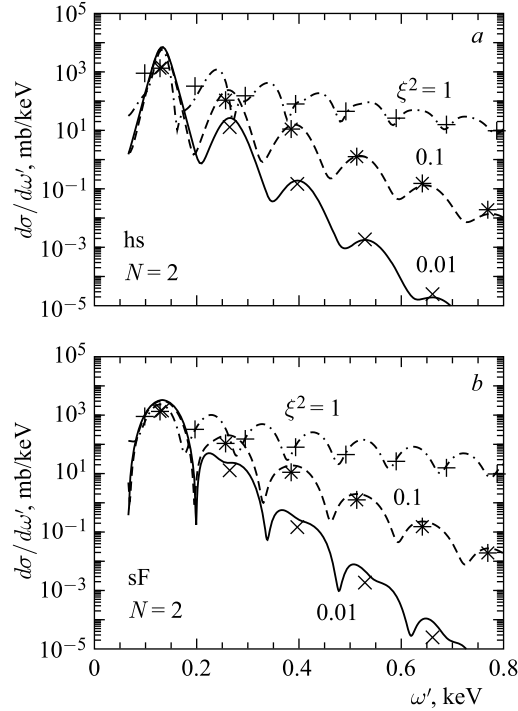


Fig. 25. Differential cross section  $d\sigma/d\omega'|_{\theta'=170^\circ}$  of the Compton scattering for  $\xi^2 = 0.01, 0.1, \text{ and } 1$ , shown by solid, dashed, and dash-dotted curves, respectively, for  $N = 2$ . The crosses, stars and pluses depict the IPA results for the lowest harmonics for  $\xi^2 = 0.01, 0.1, \text{ and } 1$ , respectively. Panels *a* and *b* correspond to hyperbolic secant (hs) and symmetrized Fermi (sF) shapes of the envelopes

oscillations show up in the cross section as some secondary bumpy structures. These properties are manifest in Fig. 24, *b*: the overall decrease of the cross section decreases with decreasing pulse duration, and the number of the secondary bumps in the region of  $\omega'$ , corresponding to the nearest integer values of  $l$ , increases with pulse duration.

In Fig. 25, we present the differential cross sections for different field intensities  $\xi^2 = 0.01, 0.1, \text{ and } 1$ , depicted by solid, dashed, and dash-dotted curves, respectively. The duration of the pulse corresponds to  $N = 2$ . The bump positions for FPA in Fig. 25 are shifted relative to the discrete positions of contributions from the individual harmonics in IPA, shown by corresponding symbols. These shifts are a consequence of the electron dressing in IPA which depends on  $\xi^2$ .

For completeness, in Fig. 26 we exhibit the differential cross sections for a subcycle pulse with  $N = 0.5$  for  $\xi^2 = 10^{-3}$  and 1, shown by solid and dash-

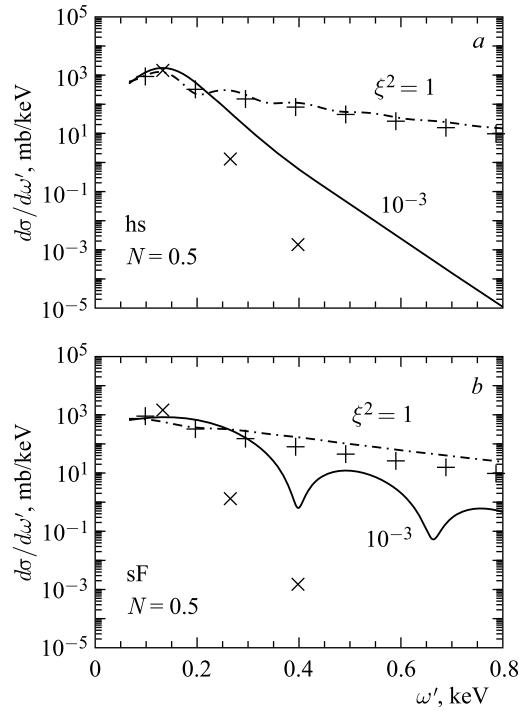


Fig. 26. Differential cross section  $d\sigma/d\omega'|_{\theta'=170^\circ}$  of the Compton scattering for  $\xi^2 = 10^{-3}$  and 1 shown by solid and dash-dotted curves, respectively, for  $N = 0.5$ . Crosses and pluses depict the discrete IPA results for the lowest harmonics for  $\xi^2 = 10^{-3}$  and 1, respectively. Panels *a* and *b* correspond to hyperbolic secant (hs) and symmetrized Fermi (sF) envelope shapes

dotted curves, respectively, for the hs (plot *a*) and sF (plot *b*) envelope shapes. Crosses and pluses depict the IPA results for  $\xi^2 = 10^{-3}$  and 1. For the hs shape, the cross sections decrease almost monotonically, with a large enhancement of the FPA result compared to IPA for small field intensities ( $\xi^2 \ll 1$ ). In the case of the flat-top envelope, the cross section exhibits some oscillations which point to more complicated spectral properties of the flat-top envelope shape.

To summarize this part, we can conclude that the results for fully differential cross sections for IPA and FPA are quite different. In IPA, the cross section represents the discrete spectrum where the frequencies of the outgoing photons  $\omega'$  are fixed according to Eq.(75). In FPA, the differential cross sections are continuous functions of  $\omega'$ . Some similarities of IPA and FPA can be seen in the case of small field intensities  $\xi^2 \ll 1$  and the smooth one-parameter envelope shape with  $N = 2-10$ . Here, the differential cross sections have a bump structure, where the position of bumps and bump heights are close to that of IPA. The situation changes drastically for more complicated (and probably more realistic) flat-top envelope shapes. In this case one can see a lot of additional bumps which reflect the more complicated spectral properties of the flat-top shape; it is difficult to find a relation not only between IPA and FPA, but also within FPA for different pulse durations. Experimentally, studying multiphoton effects, the use of rapidly oscillating fully differential cross sections seems to be rather complicated. An analysis of integral observables helps one to overcome this problem. In particular, the partially integrated cross sections have a distinct advantage: they are smooth functions of  $\omega'$  and allow one to study directly the multiphoton dynamics.

**3.3. Partially Integrated Cross Sections.** The nonlinear dynamics becomes most transparent in the partially energy-integrated cross section defined in Eq.(77). In this case, the subthreshold multiphoton events are filtered when the lower limit of integration  $\omega'$  exceeds the threshold value  $\omega'_1 = \omega'(n = 1, \xi^2)$  (with  $\xi^2 \ll 1$  for the pure Klein–Nishina process). Thus, events with  $\omega'(l) \gg \omega'_1$  and  $l \gg 1$  correspond essentially to multiphoton process, where the energy  $l\omega \gg \omega$  is absorbed from the pulse. Experimentally, this can be realized by an absorptive medium which is transparent for frequencies above a certain threshold  $\omega'$ . Otherwise, such a partially integrated spectrum can be synthesized from a completely measured spectrum. Admittedly, the considered range of energies with a spectral distribution uncovering many decades is experimentally challenging.

The partially integrated cross sections of Eq.(77) are presented in Fig. 27. The thin solid curve (marked by dots) depicts IPA results given by

$$\tilde{\sigma}^{\text{IPA}}(\omega') = \int_{\nu'(\omega')}^{\infty} dl \sum_{n=1}^{\infty} \frac{d\sigma_n^{\text{IPA}}}{d\omega'_n} \frac{d\omega'_n}{dn} \theta(n-l), \tag{79}$$



where  $\omega'(n)$  is defined by Eq. (75). That is, the partially integrated cross section becomes a step-like function, where each new step corresponds to the contribution of a new (higher) harmonic  $n$ , which can be interpreted as  $n$ -laser photon process. Results for the finite pulse exhibited by solid, dashed, and dash-dotted curves correspond to  $N = 2, 5,$  and  $10,$  respectively. In the above-threshold region with  $\omega' \leq \omega'_1$ , the cross sections do not depend on the widths and shapes of the envelopes, and the results of IPA and FPA coincide. The situation changes significantly in the deep subthreshold region, where  $\omega' > \omega'_1$  ( $l \gg 1$ ),  $n \gg 1$ . For short pulses with  $N \simeq 2$ , the FPA results exceed that of IPA considerably, and the excess may reach several orders of magnitude, especially for the flat-top envelope shown by the solid curve in Fig. 27, *b*. However, when the number of oscillations in a pulse increases ( $N \gtrsim 10$ ) there is a qualitative convergence of FPA and IPA results, independently of the pulse shape. Thus, at  $N = 10$  and  $\omega' = 0.6$  keV, the difference between predictions for hs and sF shapes is a factor of two, as compared

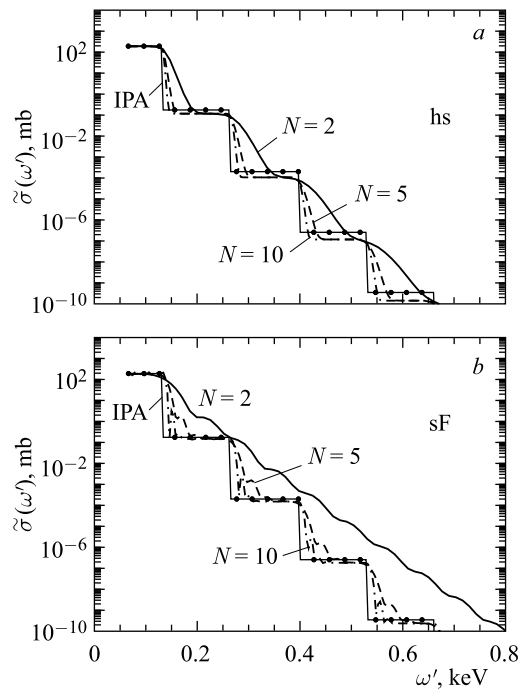


Fig. 27. The partially integrated cross section (77) for  $\xi^2 = 10^{-3}$ . The thin solid curve marked by dots depicts the IPA result. The solid, dashed, and dash-dotted curves correspond to  $N = 2, 5,$  and  $10,$  respectively. Panels *a* and *b* are for hyperbolic secant (hs) and symmetrized Fermi (sF) envelopes

with the difference of the few orders of magnitude at  $N = 2$  for the same value of  $\omega'$ .

To highlight the difference of the hs and sF (flat-top) shapes for short pulse, we exhibit in Fig. 28, *a* results for  $N = 2$ . At  $\omega' \gtrsim 0.6$  keV, the difference between them is more than two orders of magnitude.

Consider now the case of subcycle pulses with  $N < 1$ . Our result for  $N = 0.5$  is exhibited in Fig. 28, *a*. One can see a large enhancement of the cross section with respect to the IPA case for the subcycle pulse in the sub-threshold region. The enhancement for the sF shape is much greater pointing to a sensible dependence on the actual pulse shape. For a qualitative estimate of such a behavior we can drop the  $\phi_{e'}$  dependence by taking  $\phi_{e'} = 0$ . This choice is quite reasonable for the flat-top sF envelope shape and may serve as an upper limit for the cross sections in the case of the smooth hs envelope

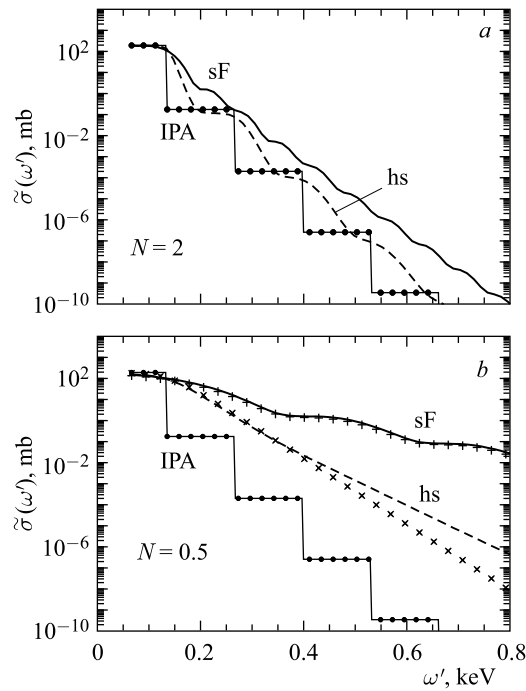


Fig. 28. The partially integrated cross section (77) for  $\xi^2 = 10^{-3}$ . *a*)  $N = 2$ , for the hyperbolic secant (hs, dashed curve) and symmetrized Fermi (sF, solid curve) shapes. *b*) The same as in panel *a*, but for a subcycle pulse with  $N = 0.5$ . The crosses and pluses correspond to the asymptotic solutions for hs and sF shapes, respectively, described in the text

shape. Under the considered conditions, the basic function  $Y_l$  in Eq. (28) can be approximated as

$$Y_l \simeq \frac{1}{2\pi} e^{-il\phi_0} \int dq F(q) \int d\phi e^{i(l-q)\phi - i\mathcal{P}(\phi)} \simeq \frac{1}{2\pi} \int dq F(q) \int d\phi e^{i(l-q-l\beta\xi)\phi - i\delta} = e^{-i\delta} F(\tilde{l}), \quad (80)$$

where  $F(l)$  is the Fourier transform of the envelope function,  $\tilde{l} = l(1 - \beta\xi)$  with  $\beta = 2\sqrt{\frac{u}{u_l} \left(1 - \frac{u}{u_l}\right)} < 1$  and  $\delta = z \int_{-\infty}^0 d\phi \cos \phi f(\phi) - l\phi_0$ . As a result, the cross section is almost completely defined by the square of the Fourier transforms (cf. Eqs. (38)), i.e.,  $\tilde{\sigma}(\omega') \simeq g(l(\omega')) F^2(\tilde{l}(\omega') - 1)$ , where  $g(\omega')$  is a smooth function of  $l = l(\omega')$  (cf. Eq. (86)). The Fourier transform for the sF shape decreases slower with increasing  $l$ . Such a dependence is evident in Fig. 27, *b*. For an illustration, the crosses depict the result of a calculation, where the basic functions  $Y_l$  and  $X_l$  in the partial probability  $\omega'(l)$  in Eq. (72) are replaced by their asymptotic values  $F^{(1)}(\tilde{l} - 1)$  and  $F^{(2)}(\tilde{l} - 1)$ , respectively. A more detail discussion of the asymptotic result is presented below (cf. Eq. (86)).

The dependence of the partially integrated cross section as a function of  $\xi^2$  at fixed ratio  $\kappa \equiv \omega'/\omega'_1 = 3$  for short pulses with  $N = 0.5$  and 2 is exhibited in Fig. 29, *a* and *b*, respectively. Note that the minimum value of  $l'(\omega')$  is related to  $\kappa$  as

$$l'(\omega') = \kappa \frac{E + |\mathbf{p}| \cos \theta'}{E + |\mathbf{p}| \cos \theta' + \omega(1 - \kappa)(1 - \cos \theta')}, \quad (81)$$

meaning  $l' < \kappa$ . Similarly, for  $n_{\min}$  one has  $n_{\min} = x$ , for  $I(x) = x$  and  $n_{\min} = x + 1$  for  $I(x) < x$  with

$$x = \frac{E + |\mathbf{p}| \cos \theta' + \frac{\omega m^2 \xi^2}{2(k \cdot p)} (1 - \cos \theta')}{E + |\mathbf{p}| \cos \theta' + \omega \left(1 - \kappa + \frac{m^2 \xi^2}{2(k \cdot p)}\right) (1 - \cos \theta')}. \quad (82)$$

The solid curves and symbols correspond to IPA and FPA, respectively, with different pulse shapes. One can see that the main difference of IPA and FPA, as well as the pulse shape dependence, appears at small field intensities  $\xi^2 \ll 1$ , where the dependence of the cross section on the pulse shape and duration is essential.

To explain this result, we use the asymptotic solution for  $\tilde{\sigma}$  which is obtained by keeping leading terms in  $\xi^2$  in Eqs. (72) and (73) and taking into account that the dominant contribution to the integrals of Eqs. (77) and (79) stems from

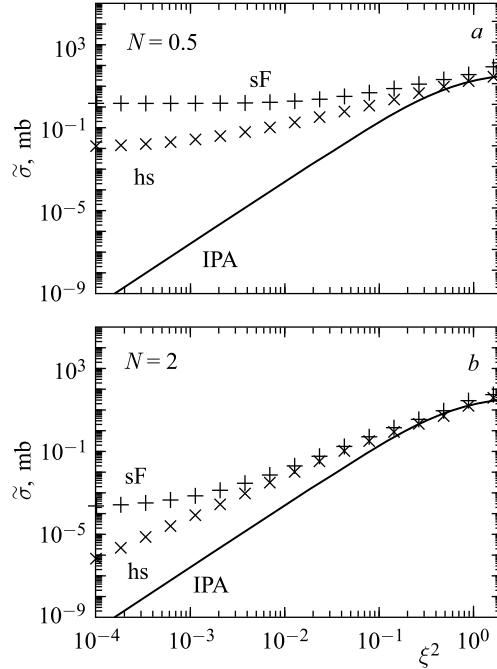


Fig. 29. The partially integrated cross section as a function of  $\xi^2$  at  $\kappa = \omega'/\omega'_1 = 3$  for short pulses with  $N = 0.5$  (a) and 2 (b). The solid curve and symbols correspond to IPA and FPA (hs and sF envelope functions), respectively

$l \sim l'$  and  $n \sim I(l') + 1$ , respectively. Consider first the partially integrated cross section in IPA. Using the asymptotic expression for the Bessel functions

$$J_k(z) \simeq \left(\frac{z}{2}\right)^k \frac{1}{k!} \quad \text{for } z \ll 1 \quad (83)$$

and keeping the leading terms in Eq. (73) with  $J_{n-1}^2(z)$  and  $n = I(l') + 1$ , one obtains

$$\tilde{\sigma}^{\text{IPA}} \simeq \frac{2\pi\alpha^2}{(E + |\mathbf{p}| \cos \theta')|\mathbf{p}|} \xi^{2k} \Phi(k), \quad (84)$$

where  $k = I(l') \simeq I(\kappa)$  and

$$\Phi(k) = \frac{(k+1)^{2(k+1)}}{(k+1)!^2} (t_k(1-t_k))^{2k} \left(1 + \frac{u}{2(1+u)} - 2t_k(1-t_k)\right), \quad (85)$$

with  $t_k = u/u_k$ , where  $u = \omega'(1 - \cos \theta')/(E + |\mathbf{p}| - \omega'(1 - \cos \theta'))$  and  $u_k = 2k\omega(E + |\mathbf{p}|)/m^2$ . Within the considered kinematics,  $t_k$  does not depend on  $k$  and can be approximated by  $t_k \simeq m^2(1 - \cos \theta')/(2(E + |p| \cos \theta')(E + |p|)) \simeq 0.35$ .

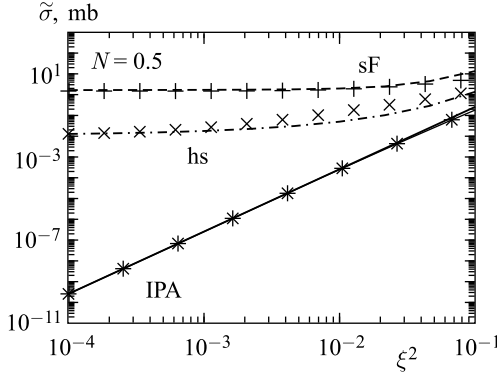


Fig. 30. The partially integrated cross sections as a function of  $\xi^2 \ll 1$  for a subcycle pulse with  $N = 0.5$ . The stars are for the full IPA result. The solid curve corresponds to the asymptotic solution of Eq. (84). The pluses and crosses are for full calculations for sF and hs shapes, respectively, while the dashed and dash-dotted curves are the corresponding asymptotic results of Eq. (86)

The result for the asymptotic solution for IPA of (84) is shown by the solid curve in Fig. 30 together with a full calculation depicted by stars. One can see an excellent agreement of these two results.

For FPA, in the case of subcycle pulse with  $N = 0.5$ , we use the asymptotic representation for the basic functions  $Y_l$  in the form of Eq. (80) which allows one to express the partially integrated cross section as

$$\tilde{\sigma} \simeq \frac{2\pi\alpha^2}{N_0(E + |\mathbf{p}| \cos \theta')} |\mathbf{p}| \times \left( 1 + \frac{u}{2(1+u)} - 2t_\nu(1-t_\nu) \right) \int_{\nu'}^{l'+1} dl F^2(\tilde{l}-1), \quad (86)$$

where  $F(x)$  is the Fourier transform of the envelope function (cf. Eq. (38)). Results for the subcycle pulse with  $N = 0.5$  are presented in Fig. 30, where the pluses and crosses are for full calculations for the sF and hs shapes, respectively. The dashed and dash-dotted curves are the asymptotic solution of Eq. (86) for sF and hs shapes, respectively.

We would like to note that, at  $\xi^2 \ll 1$ , our asymptotic solution for subcycle pulse weakly depends on  $\xi$  only through the weak  $l(1 - \beta\xi)$  dependence in the Fourier transform. The leading  $\xi^2$  dependence of the partial harmonics  $w_l$  in (72) is compensated by the  $\xi^2$  dependence of the flux factor in the denominator of Eq. (71). Nevertheless, such a weak  $\xi$  dependence is in qualitative agreement with full and asymptotic solutions, both for sF and hs envelope shapes. Thus, we can conclude that the partially integrated cross section for the subcycle pulse at  $\xi^2 \ll 1$  is almost completely determined by the square of the Fourier transform of the envelope function which is a measure of high momentum frequencies generated by the pulse shape.

In the case of a short pulse with  $N = 2$  and  $\xi^2 \leq 0.1$ , we use for the asymptotic solution the asymptotic expression of the basic functions of Eq. (37). Note that such an expression is valid only for the smooth one-parameter envelope shapes, where the function  $\mathcal{P}(\phi)$ , defined in Eq. (28), takes a simple form  $\mathcal{P}(\phi) = z \sin(\phi - \phi_0) f(\phi) + \mathcal{O}(\xi^2)$  (cf. Eq. (34)). One can see that, if the argument obeys  $l' > I(l')$ , then the main contribution to the cross section comes from the two terms with

$$Y_{k,\varepsilon_1}(z) \text{ and } Y_{k+1,\varepsilon_2}(z), \tag{87}$$

where  $k = I(l')$ ,  $\varepsilon_1 = l' - I(l') \equiv \varepsilon > 0$ , and  $\varepsilon_2 = \varepsilon - 1 < 0$ . Then, keeping the leading terms in  $\xi^2$  in (72), one can get an approximate expression for the partially integrated cross section in the form

$$\tilde{\sigma} \simeq \frac{2\pi\alpha^2}{N_0(E + |\mathbf{p}| \cos \theta') |\mathbf{p}|} \xi^{2(k-1)} \times \left( \Phi(k-1) \int_{\varepsilon}^1 d\epsilon (F^{(k)}(\epsilon))^2 + \xi^2 \Phi(k) \int_{\varepsilon-1}^1 d\epsilon (F^{(k+1)}(\epsilon))^2 \right), \tag{88}$$

where  $F^{(m)}$  is the Fourier transform of  $m$ th power of the envelope function  $f(\phi)$ . The full and approximate results for  $\tilde{\sigma}$  are shown in Fig. 31 by crosses and the dash-dotted thick curve, respectively. One can see a fairly good agreement of approximate and full results up to  $\xi^2 = 0.1$ .

In the case of the flat-top envelope, the integrand of  $\tilde{\sigma}$  has a more complicated structure with a large number of bumps. The asymptotic solution for the basic functions of Eq. (37) does not apply here. However, as a first approximation one can use the asymptotic solution of Eq. (80). Then, the cross section  $\tilde{\sigma}$  is determined by Eq. (86). The full and approximate results for  $\tilde{\sigma}$  are shown in Fig. 31 by pluses and the dashed curve, respectively. One can see an agreement of full and approximated results, however, in a very limited range of  $\xi^2 \ll 1$ .

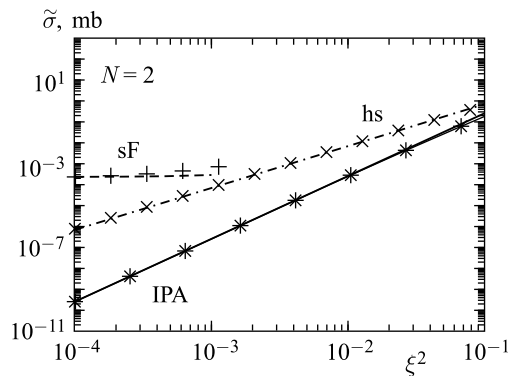


Fig. 31. Results for a short pulse with  $N = 2$ . The symbols stars, pluses and crosses are full calculations for IPA and FPA for sF and hs shapes, respectively; the solid, dashed, and dash-dotted curves are the corresponding asymptotic results of Eqs. (84), (86), and (88), respectively

To summarize this part, we note that, in the case of short pulses and small field intensities, the partially integrated cross section is determined by the interplay of pulse shape and multiphoton dynamics. For both considered shapes, the cross sections are described by the simple asymptotic expressions which can be used in practical research.

At large values  $\xi^2 \gg 1$ , our analysis shows that the dependence on the envelope shape disappears because, similar to the Breit–Wheeler process, only the central part of the envelope becomes important. Formally, under a change of the variable  $l \rightarrow l_{\text{eff}} = l + m^2 \xi^2 u / 2(k \cdot p)$ , the basic functions  $Y_l(z)$  with  $l \gg 1, z \gg 1$  become similar to the asymptotic form of the Bessel functions  $J_l(z)$  and, as a consequence, one can get the total production probability (or the total cross section) in the form of IPA [17] with a slightly modified pre-exponential factor.

**3.4. Effect of the Finite Carrier Phase.** The generalization of our approach to the case of the finite carrier phase  $\tilde{\phi}$  in e.m. potential (1) is carried out by the same method as in the case of  $e^+e^-$  pair production described in Subsec. 2.7. The functions  $C^{(i)}(l)$  in transition matrix (67) are transformed according to Eq. (60) with

$$\mathcal{P}(\phi) = z \int_{-\infty}^{\phi} d\phi' \cos(\phi' - \phi_0 + \tilde{\phi}) f(\phi') - \xi^2 \frac{u}{u_0} \int_{-\infty}^{\phi} d\phi' f^2(\phi'), \quad (89)$$

where the variables  $z$ ,  $u$ , and  $u_0$  are defined in (70). Then, using the basic functions  $Y_l(z)$  and  $X_l(z)$  in the form of Eq. (62) and utilizing Eq. (63), one can obtain the partial differential cross section  $d\sigma(l)/d\omega' d\phi_{e'}$  in the form of Eq. (71) with  $w(l)$  given by Eq. (72), but with new basic functions  $Y_l$  and  $X_l$  which now depend on carrier phase  $\tilde{\phi}$  according to Eq. (62) with (89). Recall, that  $\phi_0 = \phi_{e'}$  is the azimuthal angle of the outgoing electron momentum. The differential partially integrated cross section reads

$$\frac{d\tilde{\sigma}(\omega')}{d\phi_{e'}} = \int_{\omega'}^{\infty} d\bar{\omega}' \frac{d\sigma(\bar{\omega}')}{d\bar{\omega}' d\phi_{e'}}. \quad (90)$$

It is natural to expect that the effect of the finite carrier phase essentially appears in the differential cross section of the generalized Compton scattering as a function of the azimuthal angle of the outgoing electron momentum because the carrier phase is included in the expressions for the basic functions (62) in the combination  $\phi_{e'} - \tilde{\phi}$ .

As an example, in Fig. 32, *a* we show the differential cross section (90) as a function of the azimuthal angle  $\phi_{e'}$  for different values of the carrier phase  $\tilde{\phi}$  for the subcycle pulse with  $N = 0.5$  for the hyperbolic secant shape with

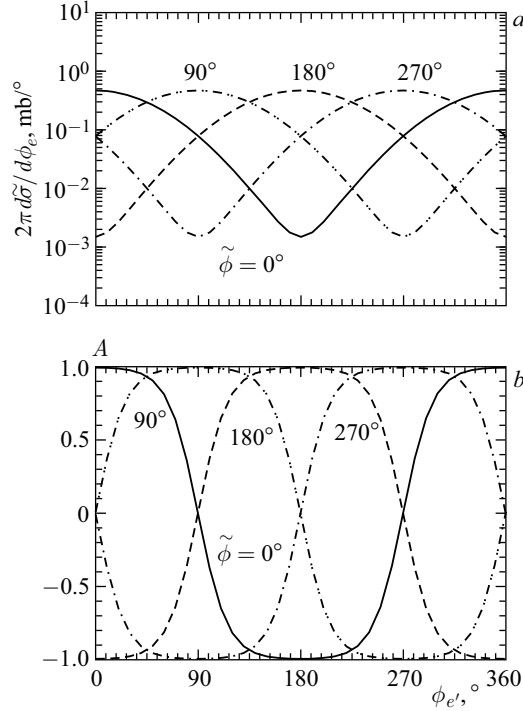


Fig. 32. *a*) The differential cross section (90) as a function of the azimuthal angle of the outgoing electron momentum  $\phi_{e'}$  for different values of the carrier phase  $\tilde{\phi}$ . The solid, dot-dot-dashed, dashed, and dash-dotted curves correspond to the carrier phase equal to 0, 90, 180, and 270°, respectively. *b*) The anisotropy (58) as a function of  $\phi_{e'}$  for different  $\tilde{\phi}$ . For the hyperbolic secant shape with  $N = 0.5$ ;  $\xi^2 = 0.1$  and  $\kappa = \omega'/\omega'_1 = 4$

$\kappa = \omega'/\omega'_1 = 4$  and  $\xi^2 = 0.1$ . One can see a clear bump-like structure of the distribution, where the bump position coincides with the corresponding value of the carrier phase. The reason of such a behaviour is the same as an alignment of the probability along  $\phi_e = \tilde{\phi}$ , described in Subsec.2.7. Corresponding anisotropies defined as

$$\mathcal{A} = \frac{d\tilde{\sigma}(\phi_{e'}) - d\tilde{\sigma}(\phi_{e'} + \pi)}{d\tilde{\sigma}(\phi_{e'}) + d\tilde{\sigma}(\phi_{e'} + \pi)} \quad (91)$$

are exhibited in Fig. 32, *b*. One can see a strong dependence of the anisotropy on the carrier phase which follows to the bump-like behavior of the differential probabilities shown in Fig. 32, *a*. Similar to the Breit–Wheeler process, the anisotropy takes a maximum value  $\mathcal{A} \simeq 1$  at  $\phi_{e'} = \tilde{\phi}$  and  $|\mathcal{A}| < 1$  at  $\phi_{e'} \neq \tilde{\phi}$ . It takes a minimum value  $\mathcal{A} \simeq -1$  at  $\phi_e - \tilde{\phi} = \pm\pi$ .



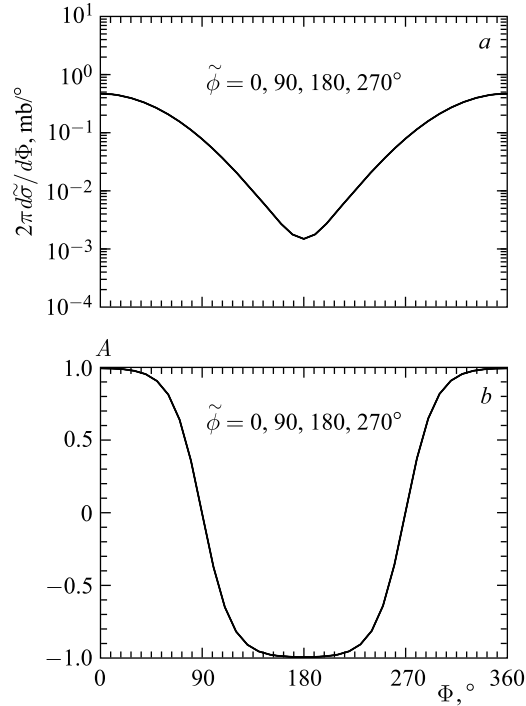


Fig. 33. The same as in Fig. 32, but as a function of the scale variable  $\Phi = \phi_{e'} - \tilde{\phi}$

The differential cross sections and anisotropies as functions of the “scale” variable  $\Phi = \phi_{e'} - \tilde{\phi}$  at fixed values of  $\tilde{\phi}$  are exhibited in Fig. 33, *a* and *b*, respectively. All curves shown in the left and right panels in Fig. 33, *a* and *b*, are merged into a single carrier phase independent curve. Similar to the Breit–Wheeler process, such a carrier phase independence of the differential cross sections and anisotropies is a consequence of the  $\phi_0 - \tilde{\phi} = \phi_{e'} - \tilde{\phi}$  dependence of the basic functions in Eqs. (62) and (63).

The effect of the carrier phase decreases with increasing pulse duration. Taking into account the similarity between Breit–Wheeler and the Compton scattering processes, we do not show here the result for the Compton scattering (for  $N \geq 2$ ), limiting to the most striking example of subcycle pulse, exhibited in Figs. 32 and 33.

#### 4. SUMMARY

In summary, we have considered two elementary quantum processes occurring in a short and intense electromagnetic (laser) pulses. They are the  $e^+e^-$  pair production (generalized Breit–Wheeler process) and the crossed process, i.e.,

emission of single photon off an electron (generalized Compton scattering). We emphasized the very significant impact of the temporal pulse structure. Still, the pulses are approximated by plane waves, meaning that curved wave fronts deserve in future also dedicated investigations.

The pair production in the subthreshold region with  $\zeta > 1$  is currently a subject of great interest. We have shown that the production probability is determined by a nontrivial interplay of two dynamic effects. The first one is related to the shape and duration of the pulse. The second one is the nonlinear dynamics of charged particles in the strong electromagnetic field itself, independently of the pulse geometry. These two effects play quite different roles in two limiting cases. The pulse shape effects are manifested clearly at small values of the product  $\xi\zeta$ , where  $\xi$  characterizes the laser intensity and  $\zeta$  refers to the threshold kinematics. The rapid variation of the e.m. field in a very short pulse amplifies the multiphoton events, and moreover, the probability of multiphoton events in the finite pulse approximation (FPA) can exceed the prediction of the infinite pulse approximation (IPA) by orders of magnitude. Thus, for example, in the case of an ultrashort (subcycle) pulse with the “number of oscillations”  $N$  in the pulse less than one, the production probability as a function of  $\zeta$  is almost completely determined by the square of the Fourier transform of the pulse envelope function. High- $l$  components, where  $l$  is the Fourier conjugate to the invariant phase variable  $\phi$ , lead to the enhancement of the production probability. Among the considered envelope shapes, the flat-top shape with fast ramping and deramping intervals is most promising to obtain the highest probability. We also find that the different envelope shapes lead to anisotropies of the electron (positron) emission which can be studied experimentally. For short pulses with  $N < 10$ , the effects of the pulse shape are also important and the final yield differs significantly from the IPA prediction. This difference depends on the envelope shapes and the pulse duration.

Contrary to that, the nonlinear multiphoton dynamics of  $e^+e^-$  production in a strong electromagnetic field plays a crucial role at large field intensities,  $\xi^2 \gg 1$ . Here, the effects of the pulse shape and duration disappear since the dominant contribution comes from the central part of the envelope function. As a result, the probabilities in FPA and IPA coincide.

In the transition region of intermediate intensities  $\xi^2 \sim 1$ , the probability is determined by the complex interplay of both the effects, and they must be taken into account simultaneously by a direct numerical evaluation of the multidimensional integrals with rapidly oscillating integrands.

The effect of the carrier phase manifests itself most clearly in ultrashort (subcycle) pulses in azimuthal distributions of direction of flight of the outgoing electron (positron). The production probability has a bump-like structure where the bump position coincides with the value of carrier phase. This leads to a definite alignment of the differential cross section and anisotropy in the  $x - y$

plane along the angle equal to the carrier phase. The impact of the carrier phase decreases with increasing pulse duration.

The considered generalized nonlinear (multiphoton) Compton scattering in short and ultrashort (subcycle) laser pulses is a crossing channel to the Breit–Wheeler process and, therefore, reflects the main features of the latter one. We have shown that the fully differential cross section as a function of the frequency of the outgoing photon at fixed production angle is a rapidly oscillating function for short pulses with the duration determined by the number of oscillations  $N = 2–10$ , especially for the flat-top envelope shapes. An experimental study of multiphoton effects in the case of rapidly oscillating cross sections seems to be rather challenging. To overcome the problem of such a staggering, we suggest to utilize the partially integrated cross section which seems to be a powerful tool for studying the nonlinear (multiphoton) dynamics in the subthreshold region. We find that these cross sections at selected pulse properties (field intensity, pulse duration) are very sensitive to the pulse shape. In the case of small e.m. field intensities, the cross section may be enhanced by several orders of magnitude as compared to an infinitely long pulse. Such an enhancement is more important for flat-top envelope shapes which generate intensive high-frequency harmonics and play a role of a power amplifier. In the above-threshold region, the partially integrated cross section manifest some “universality”, i.e., an independence of the pulse shape structure, where results for FPA and IPA are close to each other. Note that such a “universality” does not appear in fully differential cross section, where one can find rapidly oscillating cross section as a function of  $\omega'$ , especially for the flat-top envelope shape. At high field intensity, the central part of envelopes becomes dominant and the integrated cross sections coincide with that for infinitely long pulses. It provides a rationale for the use of simple analytical expressions of IPA for Monte Carlo transport approaches. Finally, we have shown that the effect of the carrier phase is important and might be seen clearly in subcycle pulses. Similarly to the Breit–Wheeler process, we predict a definite alignment of the differential cross section and anisotropy in the  $x$ – $y$  plane along the angle equal to the carrier phase.

Our considerations are focused on circularly polarized photon beams. However, we expect that qualitatively, in the case of a linearly polarized pulse, our main results, i.e., the sensitivity of the production probability of pair production and partially integrated cross section of the Compton scattering to the subthreshold multiphoton interactions and to the pulse structure, would be similar. The main difference is expected for the anisotropies since the momentum of the outgoing electron will be correlated with the direction of pulse polarization.

Our considerations are devoted essentially to the elementary processes in optical laser beams. With the availability of X-ray beams (XFELs cf. (LCLS, SACLA, European XFEL, Swiss XFEL, . . .)) already now or in the near future a

further field of interesting phenomena is entered, where the here presented theory also applies.

**Acknowledgements.** The authors acknowledge fruitful discussions with D. Seipt, T. Nousch, T. Shibata, R. Sauerbrey, and T. E. Cowan.

**Appendix**

**PRODUCTION PROBABILITY AT LARGE VALUES OF  $\xi$**

The total probability  $W$  in the limit of large  $\xi$  and small  $\xi/\zeta$ , was evaluated by Narozhny and Ritus [15] and summarized by Ritus [17] in compact form. Below, for completeness and easy reference, we recall some details of Ritus’s evaluation making an expansion for an arbitrary value of  $\xi/\zeta$ , applying it for the case of the finite pulse (cf. Subsec. 2.5).

In IPA, the total probability is represented as an infinite sum of partial harmonics [17]:

$$W = \frac{1}{4}\alpha M_e \zeta \sum_{n=n_0}^{\infty} \int_1^{u_n} \frac{du}{u^{3/2}\sqrt{u-1}} \{2J_n^2(z) + \xi^2(2u-1)(J_{n+1}^2(z) + J_{n-1}^2(z) - 2J_n^2(z))\}, \quad (92)$$

where  $n_0 \equiv n_{\min} = \zeta(1 + \xi^2)$ ,  $u_n = n/n_0$ , and  $J_n(z)$  is the Bessel function of the first kind (cylindrical harmonics). Using the identities

$$\begin{aligned} 2 \frac{n}{z} J_n(z) &= J_{n-1}(z) + J_{n+1}(z), \\ 2 J'_n(z) &= J_{n-1}(z) - J_{n+1}(z), \end{aligned} \quad (93)$$

the total probability takes the following form:

$$W = \frac{1}{2}\alpha M_e \zeta^{1/2} \sum_{n_0}^{\infty} \int_1^{u_n} \frac{du}{u^{3/2}\sqrt{u-1}} \times \left( J_n^2(z) + \xi^2(2u-1) \left( \left( \frac{n^2}{z^2} - 1 \right) J_n^2(z) + J_n'^2(z) \right) \right). \quad (94)$$

At large  $\xi \gg 1$ ,  $\zeta \gg 1$ ,  $n, z \gg 1$  and  $n > z$  one can replace the sum over integer  $n$  by an integral over  $dn$ , replacing, for convenience, integer  $n$  to continuous  $l$  with  $l_{\min} \equiv l_0 = \zeta(1 + \xi^2)$ . Using Watson’s asymptotic expression for the Bessel functions one finds

$$J_l \left( \frac{l}{\cosh \alpha} \right) = \frac{1}{\sqrt{2\pi l \tanh \alpha}} e^{-l(\alpha - \tanh \alpha)} + \mathcal{O} \left( \frac{1}{\xi} \right), \quad (95)$$

with  $\cosh \alpha = l/z$ . If  $l$  is large, the first term represents a good approximation irrespectively whether  $\xi/\zeta$  is small or large [51]. The corresponding derivative reads

$$J'_l(z) \simeq \sinh \alpha J_l(z) \left( 1 + \frac{1}{2l \sinh^2 \alpha \tanh \alpha} \right). \quad (96)$$

Consider first the case of small  $\xi/\zeta \ll 1$ , when the second term in (96) can be neglected. Then, the total probability becomes

$$W = \frac{e^2 M_e \zeta^{1/2}}{8\pi^2} \int_{l_0}^{\infty} dl \int_1^{u_l} \frac{du}{u^{3/2} \sqrt{u-1}} \frac{1 + 2\xi^2(2u-1) \sinh^2 \alpha}{l \tanh \alpha} e^{f(u,l)}, \quad (97)$$

where  $u_l = l/l_0$  and  $\hat{f}(u, l) = -2l(\alpha - \tanh(\alpha))$  with

$$\tanh^2(\alpha) = \frac{1 + \xi^2 \left( 1 - \frac{2u}{u_l} \right)^2}{1 + \xi^2}. \quad (98)$$

To avoid a notational confusion with respect to the standard variable  $\alpha$ , we replace below the fine structure constant by  $e^2/4\pi$ .

The two-dimensional integral is evaluated using the saddle point approximation since the function  $\hat{f}(u, l)$  has a sharp minimum at the point  $u = \bar{u}$  defined by the equation  $\hat{f}'_u(u = \bar{u}) = 0$ . That allows one (i) to expand it into the Taylor series

$$f(u, l) \simeq \hat{f}(\bar{u}, l) + \frac{1}{2} \hat{f}''_u(\bar{u}, l) (u - \bar{u})^2, \quad (99)$$

and (ii) to take the rest (smooth) part of the integrand in Eq. (97) at the point  $u = \bar{u}$  yielding

$$W = \frac{e^2 M_e \zeta^{1/2}}{16\pi^2} \int_{l_0}^{\infty} dl \mathcal{A}_0(\bar{u}, l) e^{\hat{f}(\bar{u}, l)} \int_1^{u_l} \frac{du}{\sqrt{u-1}} \exp \left[ \frac{1}{2} \hat{f}''_u(\bar{u}, l) (u - \bar{u})^2 \right], \quad (100)$$

with

$$\mathcal{A}_0(u, l) = \frac{1 + 2\xi^2(2u-1) \sinh^2 \alpha}{u^{3/2} l \tanh \alpha}. \quad (101)$$

The explicit expression

$$\hat{f}'_u(u, l) = \frac{4l_0 \sinh^2 \alpha}{\tanh \alpha} \frac{\xi^2}{1 + \xi^2} \left( 1 - \frac{2u}{u_l} \right) \quad (102)$$

leads to the solution

$$\bar{u} = \frac{u_l}{2} = \frac{l}{2l_0}, \quad (103)$$

which results in the following equalities:

$$\begin{aligned} \tanh \bar{\alpha} \equiv \tanh \alpha(\bar{u}) &= \frac{2}{\sqrt{1+\xi^2}}, \quad \sinh \bar{\alpha} = \frac{1}{\xi}, \quad \hat{f}_u''(\bar{u}, l) = -\frac{8l_0^2}{l\sqrt{1+\xi^2}}, \\ \mathcal{A}_0 &= \frac{1+2(2\bar{u}-1)}{\bar{u}^{3/2}l} \sqrt{1+\xi^2}, \quad \hat{f}(\bar{u}, l) = -2l(\bar{\alpha} - \tanh \bar{\alpha}). \end{aligned} \tag{104}$$

Using the substitutions  $u = t + 1$ ,  $a = 2(\bar{\alpha} - \tanh \bar{\alpha})$ , and  $A = (-1/2)\hat{f}''(\bar{u}, l)$ , one can rewrite Eq. (100) as

$$W = \frac{e^2 M_e \zeta^{1/2}}{16\pi^2} \int_{l_0}^{\infty} dl \mathcal{A}_0(\bar{u}, l) e^{-al - A(1-\bar{u})^2} \int_0^{\infty} dt t^{\nu-1} e^{-\beta t^2 - \gamma t}, \tag{105}$$

with  $\nu = 1/2$ ,  $\beta = A$ , and  $\gamma = 2A(1 - \bar{u})$ . The integral over  $dt$  is expressed via the parabolic cylinder function  $D_{-\nu}$

$$\int_0^{\infty} dt t^{\nu-1} e^{-\beta t^2 - \gamma t} = \left(\frac{1}{2\beta}\right)^{\nu/2} \Gamma(\nu) \exp\left(\frac{\gamma^2}{8\beta}\right) D_{-\nu}\left(\frac{\gamma}{\sqrt{2\beta}}\right), \tag{106}$$

which results in

$$W = \frac{e^2 M_e \zeta^{1/2}}{16\pi^{3/2}} \int_{l_0}^{\infty} dl \left(\frac{1}{2A}\right)^{1/4} \mathcal{A}_0(\bar{u}, l) \exp\left[-al - \frac{A}{2}(1-\bar{u})^2\right] D_{-1/2}(y), \tag{107}$$

with  $y = \sqrt{2A}(1 - \bar{u})$ . The main contribution to this integral comes from the region  $\bar{u} \sim 1$  ( $l \sim \bar{l} = 2l_0$ ) and, therefore, one can use the substitution

$$\int_{l_0}^{\infty} dl = -\frac{2l_0}{\sqrt{2A}} \int_{\sqrt{A/2}}^{-\infty} dy \approx \frac{2l_0}{\sqrt{2A}} \int_{-\infty}^{\infty} dy, \tag{108}$$

which results in

$$W = \frac{e^2 M_e \zeta^{1/2}}{16\pi^{3/2}} \left(\frac{1}{2A}\right)^{1/4} \frac{2l_0}{\sqrt{2A}} \mathcal{A}_0(\bar{u}, \bar{l}) e^{-2l_0 a} \int_{-\infty}^{\infty} dy e^{Zy - y^2/4} D_{-1/2}(y), \tag{109}$$

with  $Z = 2l_0 a / \sqrt{2A}$ . Using the identity

$$\int_{-\infty}^{\infty} dy e^{Zy - y^2/4} D_{-1/2}(y) = \sqrt{\frac{2\pi}{Z}} e^{Z^2/2}, \tag{110}$$

one can rewrite the production probability as

$$W = \frac{e^2 M_e \zeta^{1/2}}{16\pi} \sqrt{\frac{2l_0}{aA}} \mathcal{A}_0(\bar{u}, \bar{l}) \exp\left(-2l_0 a + \frac{l_0^2 a^2}{A}\right). \quad (111)$$

In order to reproduce the Ritus result [17] in terms of the kinematic factor  $\zeta$  and the field intensity  $\xi$ , one has to use the identity  $l_0 = \zeta(1 + \xi^2)$  and to represent  $a(\bar{\alpha})$  as a series for small values  $1/\xi$  utilizing the expansions

$$\begin{aligned} \bar{\alpha} &= \operatorname{arsinh} \frac{1}{\xi} \simeq \frac{1}{\xi} - \frac{1}{6\xi^3} + \frac{3}{40\xi^5}, \\ \tanh \bar{\alpha} &= \frac{1}{\sqrt{1 + \xi^2}} \simeq \frac{1}{\xi} - \frac{1}{2\xi^3} + \frac{3}{8\xi^5}, \quad \mathcal{A}_0 = \frac{3}{2\zeta\xi}, \end{aligned} \quad (112)$$

which leads to (48) with  $d = 1$ . Inclusion of the second term in (96) modifies eventually  $\mathcal{A}_0$  as

$$\mathcal{A}_0 = \frac{3}{2\zeta\xi} \left(1 + \frac{\xi}{6\zeta} \left(1 + \frac{\xi}{8\zeta}\right)\right), \quad (113)$$

yielding the result displayed in (48), which generalizes the Ritus result for arbitrary values of  $\xi/\zeta$ . We emphasize that, in the strong field regime, IPA is representative (with taking into account the pre-exponential factor  $d(\xi/\zeta)$  in (48)) since, as stressed above, pulse shape and pulse duration effects are subleading.

#### REFERENCES

1. Mourou G. A., Tajima T., Bulanov S. V. Optics in the Relativistic Regime // Rev. Mod. Phys. 2006. V. 78. P. 309–371.
2. Di Piazza A. et al. Extremely High-Intensity Laser Interactions with Fundamental Quantum Systems // Rev. Mod. Phys. 2012. V. 84. P. 1177–1228.
3. Yanovsky V. et al. Ultrahigh Intensity 300-TW Laser at 0.1 Hz Repetition Rate // Optics Express. 2008. V. 16. P. 2109–2114.
4. <http://www.clf.stfc.ac.uk/CLF/>
5. <http://www.eli-beams.eu>
6. <http://www.hiper-laser.org>
7. [https://www.ipfran.ru/english/science/las\\_phys.html](https://www.ipfran.ru/english/science/las_phys.html)
8. Cavalieri A. L. et al. Intense 1.5-Cycle near Infrared Laser Waveforms and Their Use for the Generation of Ultrabroadband Soft-X-Ray Harmonic Continua // New J. Phys. 2007. V. 9. P. 242.
9. Major Z. et al. Status of the Petawatt Field Synthesizer Pump-Seed Synchronization Measurements // AIP Conf. Proc. 2010. V. 1228. P. 117–122.

10. *Mackenroth F., Di Piazza A.* Nonlinear Compton Scattering in Ultrashort Laser Pulses // *Phys. Rev. A.* 2011. V. 83. P. 032106.
11. *Feng F. et al.* Generation of Isolated Attosecond Pulses with 20 to 28 Femtosecond Lasers // *Phys. Rev. Lett.* 2009. V. 103. P. 183901.
12. *Krausz F., Ivanov M.* Attosecond Physics // *Rev. Mod. Phys.* 2009. V. 81. P. 163–234.
13. *Reiss H.R.* Absorbtion of Light by Light // *J. Math. Phys.* 1962. V. 3. P. 59–67.
14. *Reiss H.R.* Production of Electron Pairs from a Zero-Mass State // *Phys. Rev. Lett.* 1971. V. 26. P. 1072–1075.
15. *Nikishov A.I., Ritus V.I.* Quantum Processes in the Field of a Plane Electromagnetic Wave and a Constant Field // *Sov. Phys. JETP.* 1964. V. 19. P. 529–541.
16. *Narozhny N.V., Nikishov A.I., Ritus V.I.* Quantum Processes in the Field of a Circularly Polarized Electromagnetic Wave // *Sov. Phys. JETP.* 1965. V. 20. P. 622–629.
17. *Ritus V.I.* Quantum Effects in the Interaction of Elementary Particles with an Intensive Electromagnetic Field // *J. Sov. Laser Res. (USA).* 1985. V. 6, No. 5. P. 497–617.
18. *Boca M., Florescu V.* Nonlinear Compton Scattering with a Laser Pulse // *Phys. Rev. A.* 2009. V. 80. P. 053403.
19. *Heinzl T., Seipt D., Kämpfer B.* Beam-Shape Effects in Nonlinear Compton and Thomson Scattering // *Phys. Rev. A.* 2010. V. 81. P. 022125.
20. *Seipt D., Kämpfer B.* Nonlinear Compton Scattering of Ultrashort and Ultraintense Laser Pulses // *Phys. Rev. A.* 2011. V. 83. P. 022101.
21. *Dinu V., Heinzl T., Ilderton A.* Infrared Divergences in Plane Wave Backgrounds // *Phys. Rev. D.* 2012. V. 86. P. 085037.
22. *Seipt D., Kämpfer B.* Two-Photon Compton Process in Pulsed Intense Laser Fields // *Ibid.* V. 85. P. 101701.
23. *Krajewska K., Kaminski J.Z.* Compton Process in Intense Short Laser Pulses // *Phys. Rev. A.* 2012. V. 85. P. 062102-1–062102-11.
24. *Titov A.I. et al.* Laser Pulse-Shape Dependence of Compton Scattering // *Eur. Phys. J. D.* 2014. V. 68. P. 299.
25. *Titov A.I. et al.* Enhanced Subthreshold Electron–Positron Production in Short Laser Pulses // *Phys. Rev. Lett.* 2012. V. 108. P. 240406.
26. *Titov A.I. et al.* Breit–Wheeler Process in Very Short Electromagnetic Pulses // *Phys. Rev. A.* 2013. V. 87. P. 042106.
27. *Nousch T. et al.* Pair Production in Short Laser Pulses near Threshold // *Phys. Lett. B.* 2012. V. 715. P. 246–250.
28. *Krajewska K., Kaminski J.Z.* Breit–Wheeler Process in Intense Short Laser Pulses // *Phys. Rev. A.* 2012. V. 86. P. 052104.
29. *Villalba-Chavez S., Müller C.* Photoproduction of Scalar Particles in the Field of a Circularly Polarized Laser Beam // *Phys. Lett. B.* 2013. V. 718. P. 992–997.



30. *Fedotov A. M. et al.* Limitations on the Attainable Intensity of High-Power Lasers // Phys. Rev. Lett. 2010. V. 105. P. 080402.
31. *Elkina N. V. et al.* QED Cascades Induced by Circularly Polarized Laser Fields // Phys. Rev. ST Accel. Beams. 2011. V. 14. P. 054401.
32. *Ilderton A., Johansson P., Marklund M.* Pair Annihilation in Laser Pulses: Optical vs. XFEL Regimes // Phys. Rev. A. 2011. V. 84. P. 032119.
33. *Hu H., Müller C., Keitel C. H.* Complete QED Theory of Multiphoton Trident Pair Production in Strong Laser Fields // Phys. Rev. Lett. 2010. V. 105. P. 080401.
34. *Ilderton A.* Trident Pair Production in Strong Laser Pulses // Phys. Rev. Lett. 2011. V. 106. P. 020404.
35. *Kirk J. G., Bell A. R., Arka I.* Pair Production in Counter-Propagating Laser Beams // Plasma Phys. Control. Fusion. 2009. V. 51. P. 085008.
36. *Bulanov S. V. et al.* On the Design of Experiments for the Study of Extreme Field Limits in the Interaction of Laser with Ultrarelativistic Electron Beam // Nucl. Instr. Meth. A. 2011. V. 660. P. 31–42.
37. *Ruffini R., Vereshchagin G., Xue S.-Sh.* Electron–Positron Pairs in Physics and Astrophysics: From Heavy Nuclei to Black Holes // Phys. Rep. 2010. V. 487. P. 1–140.
38. *Breit G., Wheeler J. A.* Collision of Two Light Quanta // Phys. Rev. 1934. V. 46. P. 1087–1091.
39. *Blaschke D. B. et al.* Properties of the Electron–Positron Plasma Created from Vacuum in a Strong Laser Field I. Quasiparticle Excitations // Phys. Rev. D. 2013. V. 88. P. 045017.
40. *Schwinger J. S.* On Gauge Invariance and Vacuum Polarization // Phys. Rev. 1951. V. 82. P. 664–679.
41. *Dunne G. V., Gies H., Schützhold R.* Catalysis of Schwinger Vacuum Pair Production // Phys. Rev. D. 2009. V. 80. P. 111301.
42. *Hebenstreit F., Alkofer R., Gies H.* Particle Self-Bunching in the Schwinger Effect in Spacetime-Dependent Electric Fields // Phys. Rev. Lett. 2011. V. 107. P. 180403.
43. *Mackenroth F., Di Piazza A., Keitel C. H.* Determining the Carrier-Envelope Phase of Intense Few-Cycle Laser Pulses // Phys. Rev. Lett. 2010. V. 105. P. 063903.
44. *Hebenstreit F. et al.* Momentum Signatures for Schwinger Pair Production in Short Laser Pulses with a Subcycle Structure // Phys. Rev. Lett. 2009. V. 102. P. 150404.
45. *Narozhnyi N. B., Fofanov M. S.* Photon Emission by an Electron in a Collision with a Short Focused Laser Pulse // J. Exp. Theor. Phys. 1996. V. 83. P. 14–23.
46. *Heinzl T., Ilderton A.* A Lorentz and Gauge Invariant Measure of Laser Intensity // Opt. Commun. 2009. V. 282. P. 1879–1883.
47. *Burke D. L. et al. (Collab.: SLAC E-144 Experiment).* Positron Production in Multiphoton Light-by-Light Scattering // Phys. Rev. Lett. 1997. V. 79. P. 1626-1–1626-4.
48. *Grypeos M. E. et al.* Properties of Fermi and Symmetrized Fermi Functions and Applications in Nuclear Physics // Phys. Part. Nucl. 2001. V. 32. P. 779–812.

49. *Volkov D.M.* Über eine Klasse von Lösungen der Diracschen Gleichung // *Z. Phys.* 1935. V. 94. P. 250–260.
50. *Berestetskii V.B., Lifshitz E.M., Pitaevskii L.P.* Quantum Electrodynamics. 2nd Ed. Course of Theoretical Physics. V. 4. Oxford; New York: Pergamon Press Ltd, 1982.
51. *Watson G.N.* A Treatise of the Theory of Bessel Functions. 2nd Ed. Cambridge: Cambridge Univ. Press, 1944.
52. *Seipt D., Kämpfer B.* Laser-Assisted Compton Scattering of X-Ray Photons // *Phys. Rev. A.* 2014. V. 89. P. 023433.
53. *Jochmann A. et al.* High Resolution Energy-Angle Correlation Measurement of Hard X-Rays from Laser Thomson Backscattering // *Phys. Rev. Lett.* 2013. V. 111. P. 114803.
54. *Seipt D., Kämpfer B.* Asymmetries of Azimuthal Photon Distributions in Nonlinear Compton Scattering in Ultrashort Intense Laser Pulses // *Phys. Rev. A.* 2013. V. 88. P. 012127.